OPTICAL CRYOIMAGING OF CELULAR REDOX IN KIDNEYS FROM DIABETIC MICE

Sepideh Maleki

A Thesis Submitted in

Partial Fulfillment of the

Requirements for the Degree of

Master of Science

in Engineering

at

The University of Wisconsin-Milwaukee

August 2012

ABSTRACT

OPTICAL CRYOIMAGING OF CELULAR REDOX
IN KIDNEYS FROM DIABETIC MICE

by

Sepideh Maleki

The University of Wisconsin-Milwaukee, 2012
Under the Supervision of Professor Mahsa Ranji

Diabetic Nephropathy (DN) is the major single cause of end stage renal diseases (ESRD) in the United States. Diabetes is the third leading fatal disorder after cancer and heart disease [1]. It is affecting 8.3% of the residents of the United States, with a total healthcare cost of $174 billion/yr by 2010 [2].

There currently exists a need for a sensitive and specific diagnosis for temporal detection of oxidative stress (OS) in cellular metabolic levels, which plays an early role in the development of DN. The objective of this research is to use a fluorescence optical imaging technique in order to delineate temporal and spatial distribution of OS and to evaluate mitochondrial redox state in rodents kidney tissue during diabetes progression.

In this research, I investigated whether changes in the metabolic state can be used as a quantitative marker of OS progression in kidneys. Through the monitoring of autofluorescent mitochondrial metabolic coenzymes (NADH, FAD), the redox state of mitochondria can be probed in many intact organs. I have applied a device called cryoimager to measure the fluorescence intensity of these fluorophores simultaneously in 3-D. The ratio of these fluorophores, referred to as the NADH redox ratio (RR), can be

used as a quantitative metabolic marker of tissue. I examined redox states of kidneys from diabetic mice, Akita/+, Akita/+; TSP1-/- (Akita mice lacking thrombospondin-1, TSP1) with increasing duration of diabetes, and kidneys from bcl-2-deficient mice.

We detected OS shortly after the onset of diabetes by NADH RR, which increased during progression of diabetes. RR indicates a more reduced biochemical state in kidneys from diabetic mice compared with kidneys from wilde type (control) mice. Thus, cryo fluorescence redox imaging showed a quantitative marker of OS progression in kidneys from diabetic mice and demonstrated that alterations in the oxidative state of kidneys occur at different stages of diabetes.

TABLE OF CONTENTS

LIST OF FIGURES

LIST OF ABBREVIATIONS

ADP - Adenosine Diphosphate

ATP - Adenosine Triphosphate

NADH - Nicotinamide Adenine Dinucleotide

NADPH - Nicotinamide Adenine Dinucleotide Phosphate

NAD(P)H - Combination of NADH and NADPH

$FADH_2$ - Flavin Adenine Dinucleotide

OS - Oxidative Stress

RR - Redox Ratio

UV - Ultraviolet

DNA - Deoxyribose Nucleic Acid

CCD - Charged Coupled Device

DN - Diabetic Nephropathy

ESRD - End Stage Renal Diseases

ROS - Reactive Oxygen Species

BCL-2 -B Cell Lymphoma Gene

TSP - Thrombospondins

WT - Wilde Type

LN_2 - Liquid Nitrogen

PVA - polyvinyl Alcohol

H&E - Hematoxylin and Eosin

P21 - Postnatal Day 21

ACKNOWLEDGMENTS

First and foremost, I would like to express my appreciation to my graduate advisor, Dr. Mahsa Ranji, who has provided me with the opportunity to perform research in this field and supported me throughout my research with her patience and guidance. Her wisdom, knowledge, and commitment to the highest standards inspired and motivated me in this field.

Most of the results described in this thesis would not have been obtained without a close collaboration with few laboratories. I would like to thank Drs. Christine Sorenson and Nader Sheibani, University of Wisconsin-Madison, who have provided me with the tissue samples studied in this research and their guidance in the biological side of the research was invaluable to me.

I would like to sincerely acknowledge my friends and lab mates in the Biophotonics Lab for their kindness and moral support during my study. I am most grateful to Reyhaneh Sepehr and Kevin Staniszewski, whose endless help and supports made this research possible and the research life pleasant.

Lastly and most importantly, my deepest gratitude goes to my family for their love and support. My husband, Nima Jalali, who has always supported, encouraged and believed in me throughout my life. My dear mother, Fereshteh Mokhtarian, who has dedicated her life to my sister and me after my father's death. My little sister, Sahar Maleki, who always inspired me with hope and faith. In beloved memory of my father, I dedicate this thesis to his great soul.

Sepideh Maleki
University of Wisconsin-Milwaukee, August 2012

Chapter 1

Introduction and Background

1. Introduction

Spectroscopic techniques examine different types of light-tissue interactions and provide biochemical and morphological information at the molecular, cell, and tissue levels in intact organs [3]. In the past several decades, fluorescence spectroscopy has had a significant effect on many different fields of research. One field that has seen such advancement is biomedical diagnostics. Within this field, fluorescence imaging has been applied to the analysis of many different types of samples, ranging from individual biochemical species (e.g., NADH, tryptophan) in intact organs to organs of living people. These studies have given rise to new methods for the early diagnosis of various medical conditions, including diabetes, cancer, lung diseases, and many others. Fluorescence analysis, which is capable of producing quantitative measures related to the tissue health, is generally classified based upon whether or not the fluorescent species are an endogenous (naturally occurring) or exogenous (externally administrated) fluorophores [4]. Some of the most intense endogenous fluorophores involved in human and animals are the cellular metabolic pathways, which are autofluorescent species, and are the focus of this research. Two endogenous fluorophores involved in cellular metabolic pathways are Nicotinamide Adenine Dinucleotide (NADH) [5], and the Flavin Adenine Dinucleotide (FAD) [6].

Endogenous fluorophores can be structural or metabolic, that can be used for disease diagnosis (e.g., diabetes) without requiring exogenous fluorescence tags. Since cells at different disease stages possess different metabolism states, there are distinct differences in their fluorescent emission spectra. These differences in fluorescence

emission depend on at least one of the following parameters: fluorophore concentration or spatial distribution throughout the tissue, local microenvironment surrounding the fluorophores, and the particular tissue architecture [3].

We monitor metabolic state in diseases of clinically important disorders such as diabetic nephropathy, and diabetic retinopathy. The future goal of our research is to translate optical fluorescent imaging to clinical avenues, and use this method for spatiotemporal diagnosis.

1.1. My Contributions

I have studied cellular metabolic activities of the onset and progression of diabetes in rodent models using optical imaging technique. Oxidative stress (OS) happens during diabetes due to cellular dysfunction and is detectable after 4 weeks of age. I have improved an instrument called cryoimager to quantify the severity of diabetes (and OS) in mouse kidneys at different stages. This imaging device specifically measures the relative oxidation of two intrinsic fluorophores, in the cell. The ratio of these two fluorophores, the redox ratio (RR), acts as a quantitative marker of the metabolic state of the tissue. I evaluated the NADH RR by measuring the intrinsic fluorescence properties of these fluorophores. Next, I quantitatively showed the progression of OS through RR on three different diabetic mouse models. Since the fluorescence of both fluorophores is entirely dependent on its oxidation, a comparison between the fluorescence levels of each fluorophore yields to a sensitive measure of mitochondrial metabolic state.

As mentioned earlier, I have contributed in improving the design of our cryoimager system. A limitation of this device was that for some small-sized samples such as mouse eye, there existed a need for higher resolution images as well as stronger signals. In order to address this limitation, I have improved the detection section of the device, which enables the cryoimager to record higher resolution images. I specifically used a sensitive CCD camera for more accurate quantification, decreased the working distance between the tissue and lens to obtain a stronger signal, used a high-resolution lens with less distortion, and employed a smaller filter wheel between the lens and camera for higher magnification.

1.2. Biological Background

1.2.1. Cell Structure and the Mitochondrion

The basic structural and functional unit of all known living organisms is the cell. It is the smallest unit of life that is classified as a living thing, and is often called the building block of life [7]. In order to function properly and stay alive, the cells must maintain homeostasis. Homeostasis is a state in which everything within the cell is in equilibrium and functioning properly [8]. The state of homeostasis keeps the cell constant with what it needs to function. This means that in homeostasis, the waste is being transported away from the cell while it receives the nutrients it needs to continue to function. When cells are in homeostasis, they work to help the organism function properly. It is important for cells maintain homeostasis of the organism to remain healthy and because of that one of the most important factors in any biological system is cellular

and sub-cellular homeostasis [9]. Figure. 1.1 shows a diagram of the typical eukaryotic cell [10].

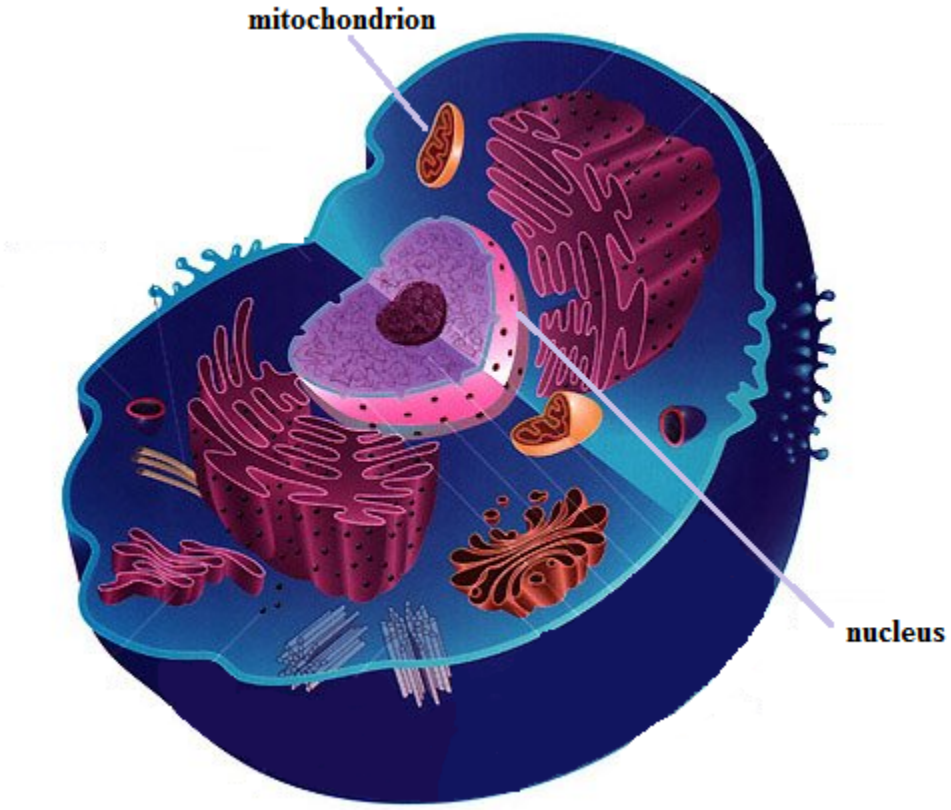

Figure 1.1. Cell Structure. Diagram of the cell including organelle [10].

The irregularities in the cell function are due to injuries and diseases within the organelles and tissue [11]. Detecting these injuries in their early stages could help in prognosis and reducing the therapies cost.

A cell consists of many cellular organelles, which are responsible for organism to remain healthy and alive, but the one responsible for energy production is the mitochondrion. Mitochondria are often referred to as the power plants of the cell since energy production takes place in mitochondria [12, 13].

A form of cellular respiration that requires oxygen in order to generate energy is termed aerobic respiration. In this process, coenzymes present in the mitochondria is oxidized and the resultant energy is ATP usable by cells [9, 14]. Therefore, the amount of energy that can be supplied to the cell is highly dependent on the amount of oxygen present in the mitochondria. The majority of energy in the cell is produced through electron transport chains, which are the cellular mechanisms used for extracting energy from redox reactions such as respiration [15]. A diagram of mitochondrial electron transport chain is shown in Figure. 1.2 [16].

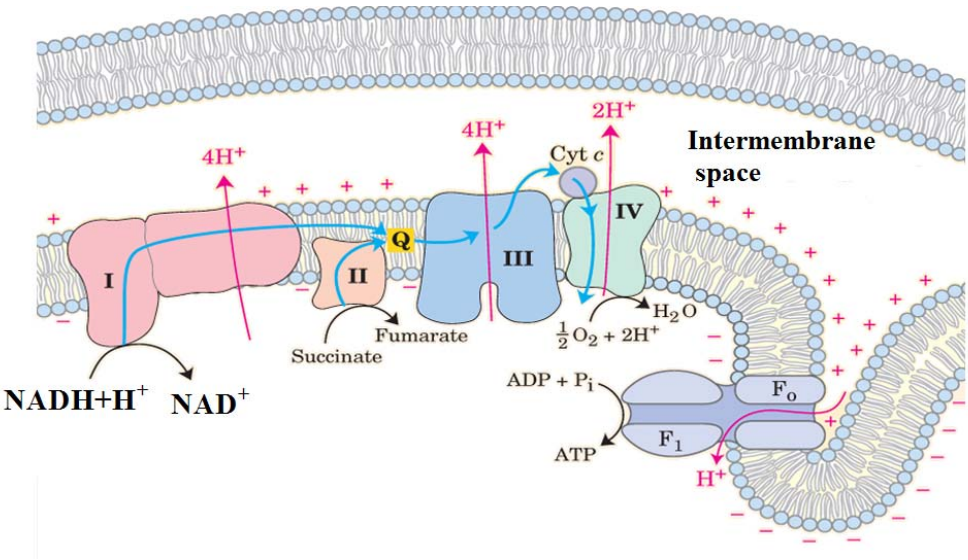

Figure 1.2. Electron Transport Chain. Simplified block diagram of the electron transport chain [16].

The electron transport chain comprises an enzymatic series of electron donors and acceptors. Each electron donor passes electrons to a more electronegative acceptor, which in turn donates these electrons to another acceptor. At the mitochondrial inner membrane, two proteins, NADH (Nicotinamide Adenine Dinucleotide) and $FADH_2$ (Flavin Adenine Dinucleotide), are oxidized through a series of protein complexes, resulting in a release of protons, which are pumped into the intermembrane space using a portion of the energy released, thus creating a proton gradient. Finally, by using the energy of the hydrogen oxidation, electric potential in conjunction with adenosine diphosphate (ADP) and inorganic phosphate results in generating adenosine triphosphate (ATP), the cell's basic unit of energy. The entire process is called oxidative phosphorylation, since ADP is phosphorylated to ATP using the energy of hydrogen oxidation in many steps [7, 17-19]. My main interest is in detecting the intrinsic fluorophore NADH and FAD in the chain.

1.2.2. Mitochondrial Oxidative Stress

In the electron transport chain reactions, a small percentage of electrons do not complete the whole series and instead directly leak to oxygen, resulting in the formation of the free-radicals, highly reactive molecules that contributes to oxidative stress and has been implicated in a number of diseases and aging. Oxidative stress (OS) is known as excess or shortage of oxygen available to the cells and is caused by an imbalance between the production of reactive oxygen and a biological system's ability to readily detoxify the reactive intermediates or easily repair the resulting damage. An excessive amount of reactive oxygen species can result in the production of peroxides and free radicals, which are capable of causing damage to all parts of a cell. Therefore, the amount

of oxygen present in and around the cell is an important factor in regulating the mitochondrial production and the rate of cell death [20-22].

The energy produced by the mitochondria can be found to be strongly dependent on the amount of oxygen available and it has been shown that a vicious circle of OS and damage to cellular structures can lead to either cell death by apoptosis or to a cellular energetic decline and ageing. Figure 1.3 shows the mitochondrial dysfunction, and eventual cell death due to increasing oxidative stress [23].

.

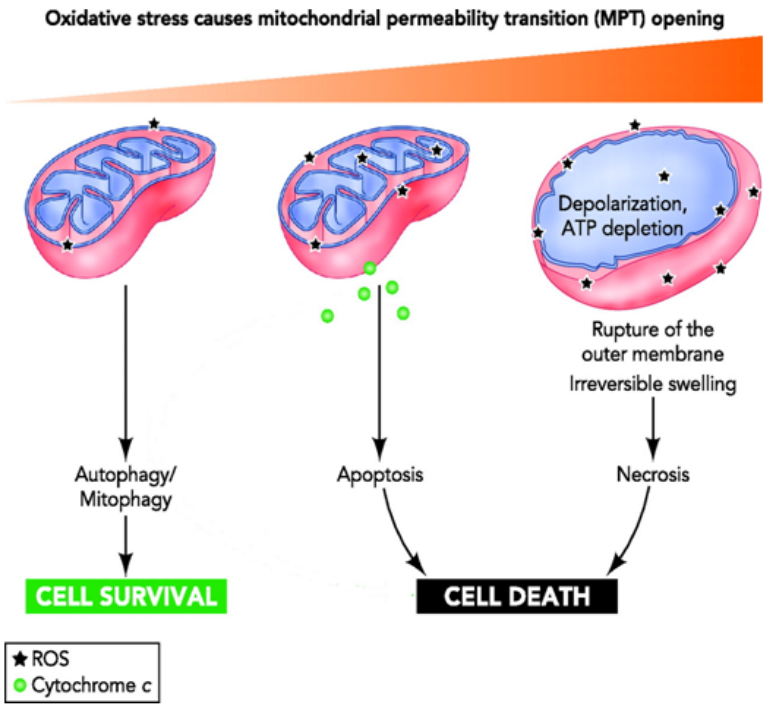

Figure 1.3. Impact of Oxidative Stress. Mitochondrial dysfunction, and eventual cell death due to increasing oxidative stress (left to right) [23].

A variety of diseases cause an improper function of the mitochondria by disrupting the balance of oxygen flow into and around cells, which results in an increased rate of cell death, via apoptosis or necrosis [24]. In many cases, the amount of oxygen available to a cell can accurately represent the health of the cell and be used as a tool for diagnosis. This is especially true in cases related to mitochondrial dysfunction or diseases related to oxidative stress, such as diabetes. In these cases, the oxidation state (redox state) of the tissue serves as a sensitive and reliable measure for evaluation of cell behavior. My goal has been on the detection of redox state as a measure of oxidative stress damage in the tissue.

1.3. Fluorescence

1.3.1. Physical Principles of Fluorescence

By definition, fluorescence is the emission of photons from a substance that has absorbed photons. In most cases the emitted light has a longer wavelength, and therefore lower energy, than the absorbed photons [5]. Fluorescence occurs when an orbital electron of a molecule, atom, or nanostructure relaxes to its ground state by emitting a photon of light after being excited to a higher quantum state by some type of energy such as bright light source or extreme heat. Since the amount of heat required to excite the molecules is typically large, a light source is commonly used for this excitation. A molecule at the excited energy state (S_1) state can relax by various pathways such as non-radiative relaxation in which the excitation energy is dissipated as heat (lattice vibration) to the solvent. Another scenario is that, a relatively small portion of the energy is lost to

lattice vibrations prior to the release of extra energy and relaxation to the ground state. There is a probability, termed the fluorescence quantum yield, which is the indicator of the efficiency of the fluorescence process. It is defined as the ratio of the number of photons emitted to the number of photons absorbed. The maximum fluorescence quantum yield is 1.0 (100%), which corresponds to every photon absorbed resulting in a photon emitted. If the photon emission occurs, a photoelectric device can quantify the amount of releasing energy. The fluorescence process can be seen in Figure 1.4 [25].

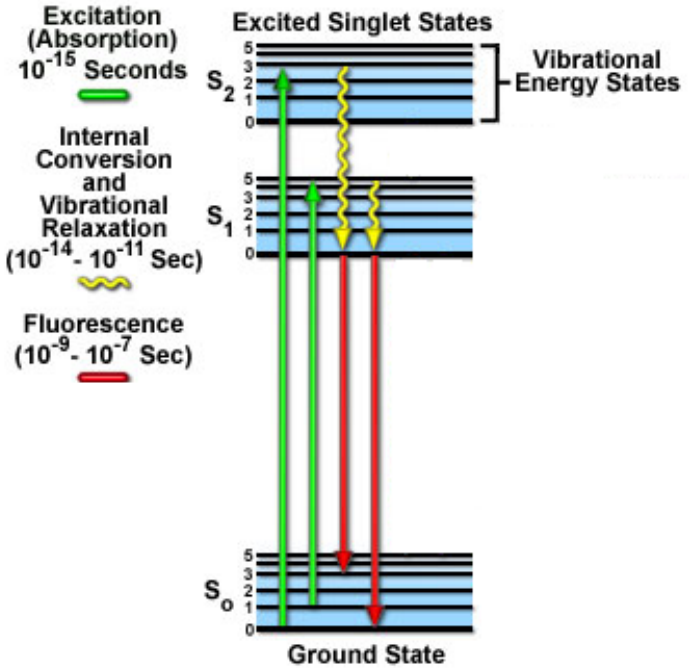

Figure 1.4. Jablonski Diagram of Fluorescence. Fluorescence as a result of molecule excitation. Green lines indicate excitation, yellow lines relaxation, and red lines emission of fluorescence [25].

For exciting many molecules, and specially the molecules that are intrinsically fluorescent corresponding to the allowed energy levels of the molecule, there is a narrow

range of light energies. Since the photon energy is in an inverse relation to its wavelength or directly proportional to the frequency of the light, only one specific range of wavelengths can be used to excite a molecule. The wavelength, or color, of the emitted fluorescence light has a narrow range since it has energy equal to the energy released when the molecular transitions back to its ground state.

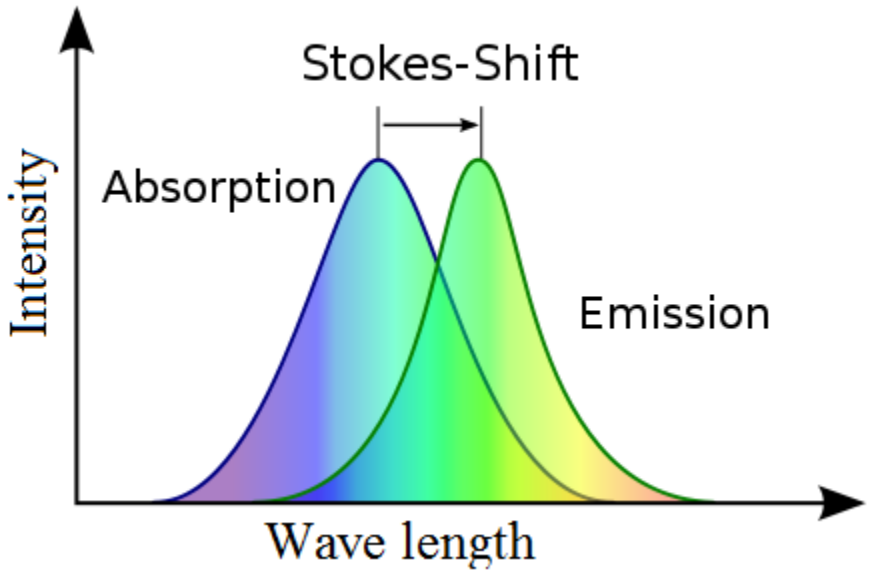

Figure 1.5. Stokes Shift. Example excitation and emission spectra of a fluorophore. The difference between absorption and emission maxima is known as the Stokes Shift [26].

When a system absorbs a photon, it gains energy and enters an excited state. One way for the system to relax is to emit a photon, thus losing its energy. When the emitted

photon has less energy than the absorbed photon, this energy difference is the Stokes shift [27] as seen in Fig. 1.5 [26].

To detect the emitted fluorescence light in this phenomenon, the excitation and emission light must be separated by using optical filters or dichroic mirrors. Although the narrow range of both the excitation and emission light would seem to be a limiting factor in the usefulness of fluorescence due to its necessitation of concentrating power into a narrower range, this actually benefits the fluorescence method in that multiple molecule can be monitored sequentially, provided that their fluorescence spectra are not completely overlapping.

1.3.2. Intrinsic Mitochondrial Fluorophores

Fluorophores are small molecules that can be part of a molecule (intrinsic) or added to a molecule (extrinsic). Intrinsic fluorophores are those that occur naturally in most tissues and they can be used as natural indicators to study the structure, the dynamics, and the metabolism of living cells. These intrinsic fluorophores include tryptophan, collagen, NADH, flavins, and porphyrins. Two of these fluorophores, NADH (Nicotinamide Adenine Dinucleotide), and Flavoprotein Adenine Dinocleotide ($FADH_2$, one of the flavins), are essential in the metabolic pathway of the mitochondria and they are located in the protein complexes one and two of the electron transport chain. These fluorophores are used to determine the oxidation state of the mitochondria [15]. In addition, these coenzymes are autofluorescent, with the spectra shown in Figure 1.6 [28, 29], in some specific biochemical states [30].

NADH, and FAD (the oxidized form of $FADH_2$) are the primary electron carriers in oxidative phosphorylation, they are autofluorescent and can be monitored without exogenous labels by optical techniques. These coenzymes are beneficial in that NADH is primarily fluorescent in its reduced biochemical state, whereas FAD is the only fluorescent in its oxidized form. Therefore, by imaging these two coenzymes, we can probe the oxidative state of the metabolism in tissue. The fluorescent signals of these intrinsic fluorophores have been used as indicators of tissue metabolism in injuries due to hypoxia [31], ischemia, and cell death [32-34]. Additionally, the normalized ratio of these fluorophores, (NADH/FAD), called the NADH redox ratio (RR), acts as a novel marker of the mitochondrial redox and metabolic state of tissue *ex vivo* and *in vivo* [34]. Although this ratio is not a direct measure of the concentrations of these fluorophores, the fluorescence intensity measured is a relative measure of their concentrations. This ratio is beneficial, as it is a quantitative marker of tissue metabolism independent of the number of mitochondria.

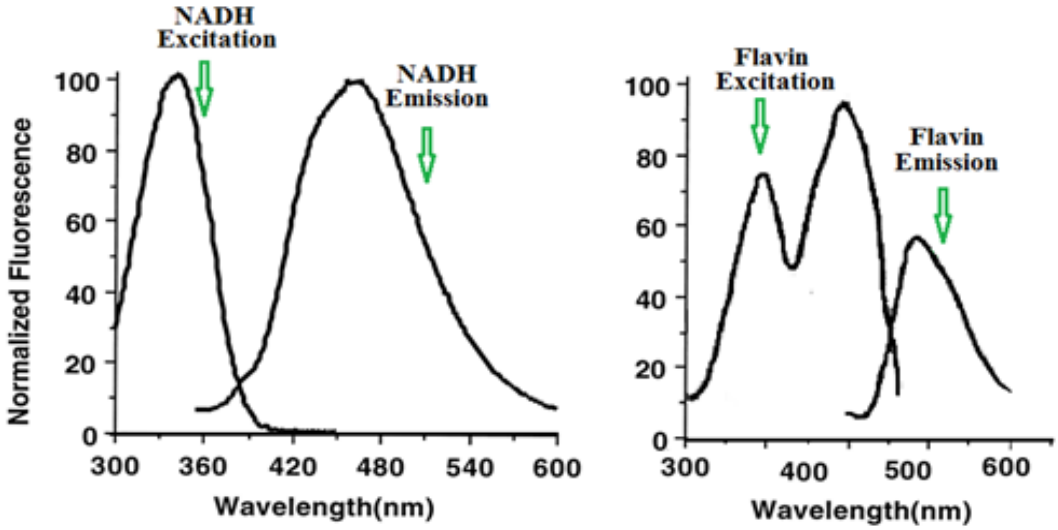

Figure 1.6. NADH and FAD Fluorescence Spectra. Excitation and emission spectra of NADH (left) and FAD (right) [28, 29].

By filtering a white light such as mercury-arc light at related excitation wavelengths, NADH and FAD can be excited. NADH has a maximum in its excitation spectrum at 340 nm (ultraviolet region of the electromagnetic spectrum) and an emission maximum at 460 nm (blue in color), and FAD has its excitation maximum at 448 nm (blue in color) and a maximum in the emission spectrum at 520 nm (green in color). There is an overlap between the NADH emission and FAD excitation, which requires the sequential excitation and detection of the two fluorophores. The selective detection of fluorescence between the two fluorophores is possible due to the fact that the excitation spectra don't overlap each other, and the emission spectra don't overlap either. Hence, the fluorescence signal of each of these fluorophores will give us a measure of the health of cells within an organ.

1.3.3. Interfering Factors

The filter sets used in the experiments allow for excitation of other endogenous fluorophores, such as collagen, elastin, and NAD(P)H in the NADH channel, and flavin mononucleotide in the FAD channel. Since the collagen and elastin fluorescence signals are constant regardless of oxidation, thus, they don't impact the change in the fluorescence signal and resultant change in the signal is due to metabolic oxidation. Flavin mononucleotide is also involved in the metabolism, and its fluorescence behaves in the same manner as FAD.

NADPH, which is an indicator of tissue oxygenation fluoresces with the same characteristics as NADH, however, detection of this enzyme is undesirable since NADPH is not related to the metabolism. Fortunately, the signal intensity of NADPH has been shown to be much less than that of NADH [34-37], and so can be considered negligible. Chance et al. demonstrated that the fluorescence signal originates mostly from NADH in the mitochondria and the contribution of NADPH is very small [38]. Other groups showed that the concentration of NADH is about 5 times greater than NADPH, the NADH quantum yield is 1.25 to 2.5 times greater than NADPH, and that metabolic diseases only affect NADH [35-37]. For these reasons, it is obvious that the changes in the redox ratio measured are due to changes in the mitochondrial redox ratio, and are not impacted by the other endogenous fluorophores present in the tissue.

1.4. Imaging Background

1.4.1. Optical Imaging

Optical imaging techniques for the assessment of tissue anatomy, physiology, metabolic, and molecular function have emerged as an essential tool for both the basic researcher and clinical practitioner. One main concern of clinical practitioners is that too much harmful radiation is used to detect diseased tissue. One main advantage of optical imaging techniques arises from the fact that endogenous and exogenous fluorescent dyes can be detected at low concentrations, without harmless radiation and can be applied repeatedly to the patient. Furthermore, the remarkable progress in the development of optical instrumentation in the last two decades has decisively contributed to the growing applicability of optical imaging tools , which have the advantage of being less harmful, inexpensive and sometime with a reasonable sensitivity and specificity [3].

The term optical imaging encompasses a large variety of different disciplines. In our fluorescence imaging method, light in the ultraviolet (UV), and the blue spectral region is used to obtain information on the biochemical characteristics of tissue. Generally, the interaction of photons with tissue is based on absorption of light, scattering of light, and emission of fluorescent. These three parameters can be used separately to characterize tissue optical properties. My focus is the third interaction, the fluorescence.

A fundamental observation for optical diagnostic procedure relates to the fact that the penetration depth of light in living tissue strongly depends on the wavelength used because the amount of absorption and scattering events in tissue is a function of wavelength [39-41].

For wavelengths below approximately 600 nm, the penetration of light into the tissue is limited to a depth of hundreds of micrometers up to a few millimeters due to strong absorption of the photons, so that only superficial assessment of tissues in this spectral region is possible. The absorption of light in tissue originates from oxy- and deoxyhemoglobin and several tissue components such as porphyrins, melanin, NADH and flavins, collagen, elastin, and lipopigments. Fluorescence of these intrinsic fluorescence markers (autofluorescence) has been studied as a source of specific spectral information on tissue structure and pathophysiological states [4, 42] and was thoroughly exploited to identify diseased tissue areas, e.g., in endoscopy [43, 44] or cardiovascular diagnosis [45].

In the past few years, remarkable optical techniques for the imaging and detection of diseases have emerged. Imaging modalities in the optical regime have the advantage of being sensitive, accessible, relatively low-cost, and rapid. The strength of optical imaging technique is that it allows for highly sensitive detection of molecular signals. In that respect, existence of endogenous or exogenous fluorophores offers various opportunities to the acquisition of optical signals. Several parameters, such as the absorption coefficient, fluorescence quantum yields, fluorescence decay times, and fluorescence quenching/recovery process, are accessible for reporting physiological states, molecular conditions, and molecular function.

1.4.2. Fluorescence Imaging

Fluorescence imaging provides specific information on tissue using intrinsic fluorophores or exogenous tagged proteins. Since some of the molecules in the cell have intrinsic fluorophores and are able to fluoresce when excited with the appropriate wavelength, a growing field of fluorescence spectroscopy and imaging techniques relies on autofluorescent fluorophores. In this method, the intrinsic fluorescence of some of the fluorophores present in the cell can be used to determine the amount of oxygen existent in the cell's environment. Fluorescence-based techniques are widely used in biomedical applications as diagnostic/therapeutic tools for early detection of various diseases and to probe tissue redox state and energy homeostasis in organs such as the heart [46], brain [47], kidney [48, 49], liver [50], skeletal muscles [51], cervix [52], and colon [53]. These techniques are widely used in biomedical applications and have been shown to have a high sensitivity and specificity for discriminating between diseased and non-diseased tissue. In this research, fluorescence imaging was used to evaluate the kidney mitochondrial redox state [49, 54].

1.5. Disease Model

1.5.1. Diabetic Nephropathy

Diabetic nephropathy (DN) is a progressive kidney disease caused by diabetes. Diabetes is classified into two types, which is: type 1 diabetes also called insulin-dependent diabetes, and type 2 diabetes, called non-insulin dependent diabetes. In type 1, the pancreas cannot produce enough insulin or produce no insulin. With limited levels of insulin produced, glucose cannot be delivered into fat, liver cells and muscle for energy, which leads to deposition of large quantities of blood glucose in the body. Then, the high level of glucose occurs accordingly. In type 2, the cells cannot respond properly to the insulin, which shows one condition that the inability of the cells to make full use of insulin [55-57].

In the kidneys, there are millions of tiny blood vessels (capillaries) with tinier holes in them, which are responsible for filtering the waste products caused by protein digestion. As blood flows through the blood vessels, small molecules such as waste products squeeze through the holes and these waste products become part of the urine. Useful substances, such as protein and red blood cells, are too big to pass through the holes in the filter and stay in the blood. High blood sugar from diabetes can destroy these blood vessels and make the kidneys filter too much blood. When diabetes damages this delicate filtering system, the result is diabetic nephropathy. Severe damage can lead to kidney failure or irreversible end stage renal disease (ESRD), requiring dialysis, or a kidney transplant [58-60].

1.5.2. Mitochondrial Dysfunction in Diabetes

Oxidation-reduction or redox reactions are pivotal to maintaining cell life through respiration, metabolism, and energy supply. Oxygen free radicals, known as super oxide (O_2), leak from the mitochondria and react with the other molecules to create reactive oxygen species (ROS). The inability of a cell's antioxidant defense to overcome oxidative injury over time will eventually lead to cell death [60, 61].

Hyperglycemia or high blood sugar is a condition in which an excessive amount of glucose circulates in the blood plasma. Excess generation of highly reactive free radicals, largely due to hyperglycemia, causes oxidative stress, which further exacerbates the development and progression of diabetes and its complications [62-64].

Diabetes can trigger excess generation of ROS and plays an important role in increasing OS in various tissues, including the kidney. When OS happens, normal cellular respiration is undergoing, resulting in dysregulated mitochondrial free radical production and disparity between ROS generation and antioxidant defenses. The combination of stress-induced and conventional mitochondrial dysfunction exacerbates the progression of disease and its associated complications such as renal vascular and proximal tubule dysfunction [65-67], cancer [68], and pulmonary diseases [69].

1.5.3. Mice Models of Diabetes

B Cell Lymphoma Gene (BCL-2)

The bcl-2 gene plays an essential role during kidney development and lack of bcl-2 (Bcl-2-/- mice) enhances apoptosis affecting kidney development and growth. Bcl-2-/- mice have a number of defects, including smaller size, and die at six weeks of age from polycystic kidney disease and renal failure. Bcl-2 plays a central role in maintaining mitochondrial oxidative homeostasis [71, 72]. In addition, bcl-2 expression is significantly decreased during diabetes [73], thus, its absence causes a more oxidized state in tissue and, as such, the mitochondria is more oxidized in bcl-2-/- mice as compared with their controls. In addition, bcl-2 is an anti-apoptotic protein whose expression decreases significantly during diabetes, and thus is of direct interest for this study.

Akita Model

The Akita mouse, which has a mutation in the insulin 2 gene, is a model for diabetes. The male Akita mouse has diabetes, while females develop mild diabetes. Akita diabetic mice develop type 1 diabetes as early as 4 weeks of age and show normal survival until 6 months of age but then show a dramatic decrease in survival with almost no survivors from 12 months of age. Enzymatic and non-enzymatic sources contribute to ROS observed in the diabetic kidneys, including advanced glycation, mitochondrial respiration chain deficiencies, and NAD(P)H oxidase [55, 74]. We have studied OS in this model by our optical imaging tools.

Thrombospondin-1 (TSP1)

Thrombospondin-1 (TSP1) is a potent endogenous inhibitor of angiogenesis, whose production is decreased during diabetes. An angiogenesis inhibitor is a substance that inhibits the growth of new blood vessels. Our hypothesis is that decreased production of TSP1 promotes the development and progression of diabetic nephropathy resulting in vascular dysfunction. To test this hypothesis the Akita/+ TSP1-/- is studied to see if lack of TSP1 exacerbates the pathogenesis of diabetic retinopathy. The Akita/+TSP1-/- mouse is a novel diabetes model that exhibits severe nephropathies with a relatively short duration of diabetes compared with the parental Akita/+ mice. Thus, the mice that carry the Akita mutation and lack TSP1 (TSP1-/-) serve as a model for severe diabetic nephropathy. Here we propose to determine the impact of the combination of these genetic modifications on the mitochondrial redox state associated with the onset and progression of diabetes. To verify that TSP1-/- genotype itself does not contribute to a more oxidized mitochondria, we compared TSP1-/- mice with Akita/+TSP1-/- mice. This provides an advantage to study most of the non-proliferative early retinopathies with a shorter duration of diabetes. Akita/+TSP1-/- mice are a novel model of diabetes in which non-proliferative diabetic retinopathy can be detected with a shorter duration of diabetes [49]. We have studied OS in this model by our optical imaging tools.

Chapter 2

Optical Cryoimaging of Diabetic Nephropathy

2. Cryoimaging

2.1. Introduction

The cryoimager is an automated image acquisition and analysis system consisting of software and hardware designed to acquire fluorescence images of tissue sections. Barlow Scientific Inc. first implemented this device for measuring the regional blood flow from fluorescent microsphere images [75, 76]. The first implementation of this device can be seen in Figure 2.1 in which a motor-driven microtome sequentially sections frozen tissue at the desired slice thickness while filtered light from a mercury arc lamp excites up to five distinct fluorophores in the exposed surface of the tissue block. At each slice, a CCD camera records a fluorescence image of the tissue block in pixel dimensions of 10μm × 10μm to later be analyzed for fluorophore distribution. The microtome is housed in a freezer unit that maintains the sample at -25°C during sample slicing and image acquisition. The resolution in the z direction (thickness of microtome slices) can be as small as 5 μm. For this study, depending on the kidney's size, different resolutions in the z direction were used. In the second design, the field of view of the device was improved to 12mm×9mm from the previous version of 65mm×45mm. Further details of each design can be found in the following section.

Cryoimaging is advantageous over the other methods since it provides a high fluorescence quantum yield of NADH and FAD as compared with room temperature, 3-D

spatial distribution of tissue NADH and FAD fluorescence intensities, and it is a 3-D fluorescence imaging technique.

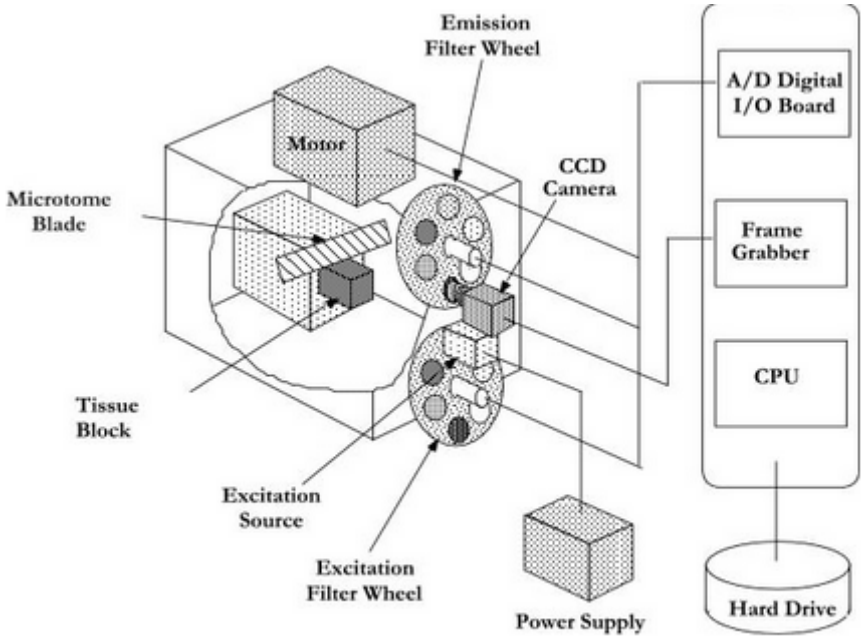

Figure 2.1. Cryoimager Design. Early design of cryoimager manufactured by Barlow Scientific inc. [75].

2.2. Optical Design

A 3-D fluorescence imaging system termed the cryoimager was used to evaluate the redox state of the metabolism in intact organs. This device uses the autofluorescence of the previously mentioned NADH and FAD co-enzymes within the mitochondria to determine the cellular redox state. By measuring the fluorescence intensities of a reduced protein, NADH, and an oxidized protein, FAD, one can obtain an effective measure of the oxidation state of the mitochondria. The use of a 3-D cryofluorescence redox imaging

technique allows for measurement of spatiotemporal 3-D fluorescence images of intrinsic and extrinsic fluorophores in intact organs.

2.2.1. Excitation Path

Excitation light is generated from a 200 W mercury-arc lamp (Figure 2.2-1; Part Number 6283NS, Newport Instrument, CT, U.S.A) resulting in a broadband, intense white light that can be used to excite multiple fluorophores.

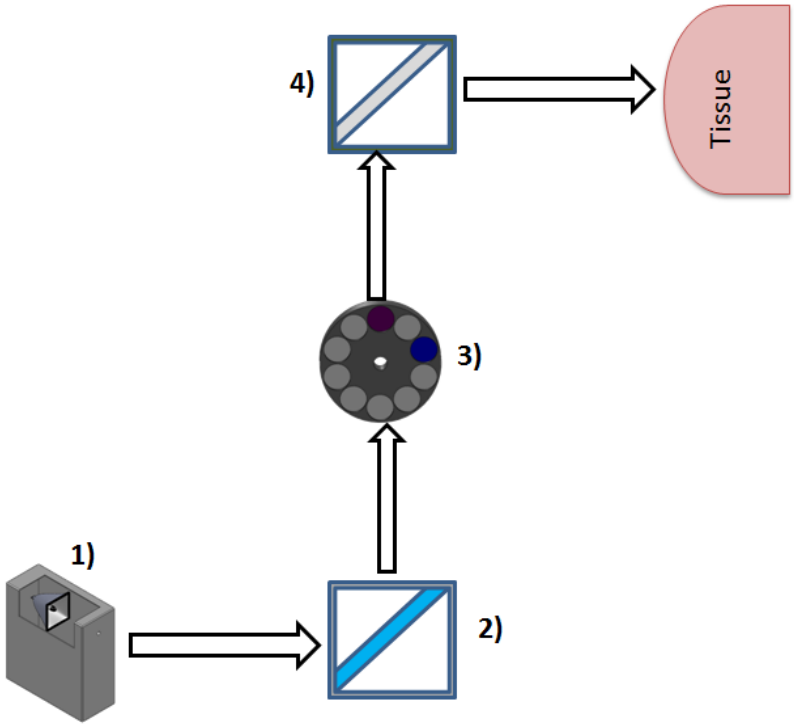

Figure 2.2. Cryoimager Excitation. Block diagram of the components which make up the excitation side of the cryoimager. 1) Mercury-arc lamp. 2) Cold mirror. 3) Filter wheel. 4) Mirror

The white light from the mercury arc lamp is then coupled into a condenser, which homogenizes the light. The light is then incident on a cold mirror (Figure 2.2-2) to get rid of the infrared portion. The homogeneous light is then delivered to a filter wheel (Figure 2.2-3). The filter wheel is then used to rotate a set of optical bandpass filters to select the proper wavelengths for excitation of each fluorophore. These optical bandpass filters allow transmission through a specified range of wavelengths, whereas light outside the transmitted range is attenuated by approximately 5 orders of magnitude, with a very narrow transition regime (< 5 nm). The excitation light was filtered at the excitation wavelength of NADH and FAD, The excitation band pass filters used for NADH is 350 nm (80 nm bandwidth, UV Pass Blacklite, HD Dichroic, Los Angeles, CA) and for FAD is 437 nm (20 nm bandwidth, 440QV21, Omega Optical, Brattleboro, VT). After passing through the appropriate filter, the excitation light, which is now a narrow range within the excitation spectrum of the desired fluorophore, is then reflected by a mirror (Figure 2.2-4), transmitted through a glass viewport, and reaches the tissue surface.

2.2.2. Detection path

After light is exposed on the tissue surface, the emitted fluorescent light is collected via passage through another filter wheel. The emitted light is then coupled into a lens and a CCD camera records a fluorescence image of the tissue block in desired pixel dimensions to be later analyzed for fluorophore distribution.

First Design

In the first design, the cryoimager was capable of low resolution images (45mm× 40 mm) for large-sized samples such as rat lung, pig heart, etc. Figure 2.3 shows a sample grid image and a slice of a rat lung sample provided by the cryoimager's initial setting. In this design, the steps are nearly the same as what was described earlier, except the detection part, which is the difference between the two designs. The lamp and the excitation filter wheel are the same in both designs but the camera, lens, emission filters, emission filter wheel, and the working distance between the tissue surface and lens were changed for different sample imaging. The working distance between the tissue surface and the lens was 38.8 cm and, because of that higher distance, a large emission filter wheel was used in between the tissue surface and the lens. The specification of the emission filters on the filter wheel is as follows: the emission filter for NADH is 460 nm (50 nm bandwidth, D460/50M, Chroma, Bellows Falls, VT) and for FAD is 537 nm (50 nm bandwidth, QMAX EM 510-560, Omega Optical, Brattleboro, VT). The lens used in this setting was a Pentax TV zoom lens (D2560997, Pentax Corporation, Japan) and images were collected with an Exi Aqua color (QImaging EXi Aqua, Canada) CCD camera. The camera features a low dark current, 6.45 micron pixels, and a high quantum efficiency.

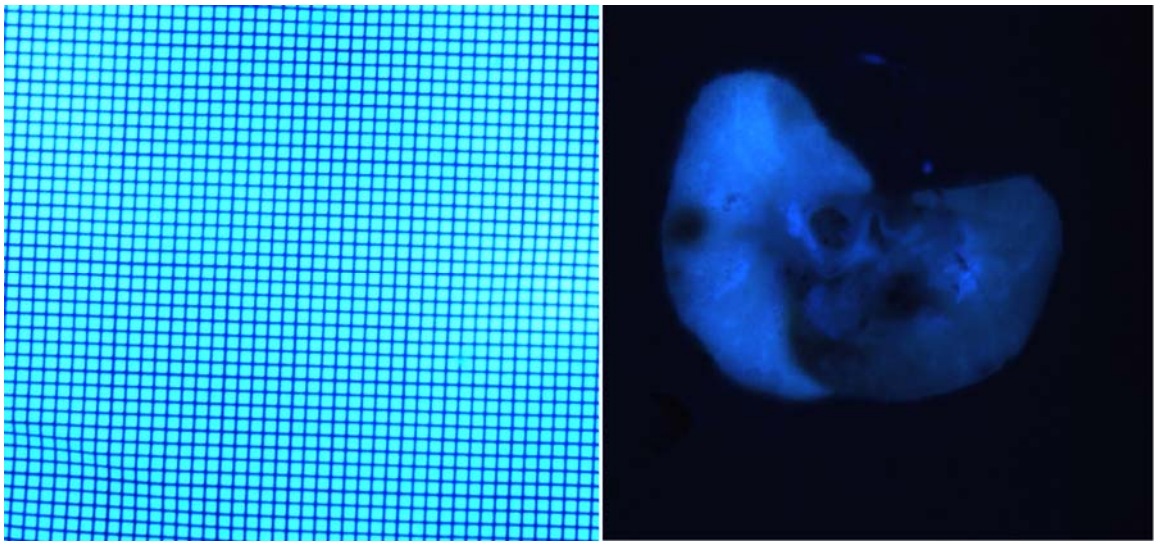

(a) (b)

Figure 2.3. Cryoimager's first design low resolution images (45mm× 40 mm). a) Grid b) A sample rat lung image

As described earlier, after light is exposed on the tissue surface, the emitted fluorescent light is collected via passage through large emission filter wheel (Figure 2.4-1). The emitted light is then coupled into pentax lens (Figure 2.4-2) and an aqua camera (Figure 2.4-3) records a fluorescence image of the tissue block.

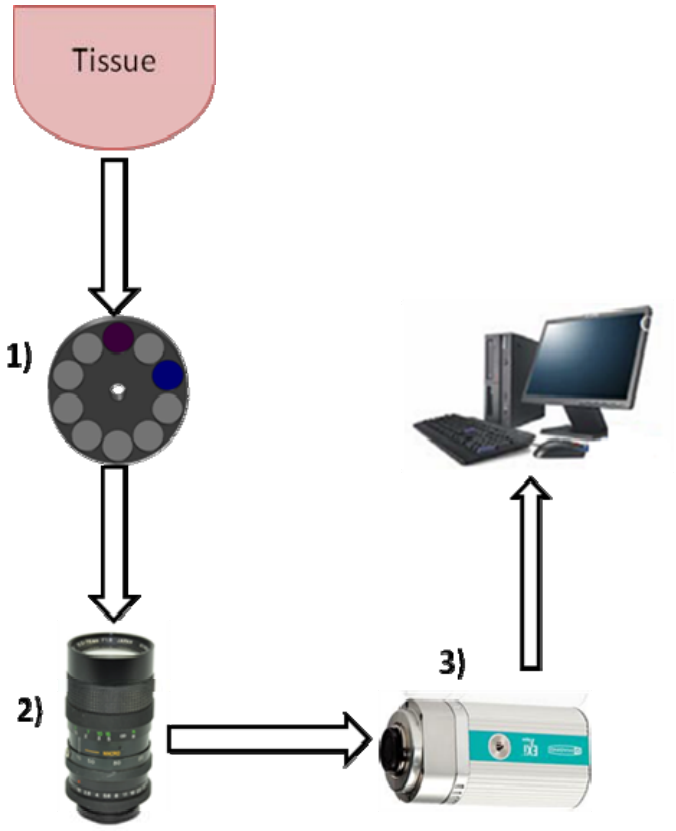

Figure 2.4. Cryoimager Detection. Block diagram of the components which make up the detection side of the cryoimager's first design. 1) Emission filter wheel. 2) Pentax lens. 3) Aqua Exi camera [77, 78].

However, there was a major disadvantage to this implementation; the system needed higher resolution and stronger signals for imaging of small-sized samples such as the mouse's eyes. We addressed this limitation by improving the detection section of the device that led to the second design explained in details in the next section.

Second Design

To improve the problem mentioned in the first design, the detection section of the cryoimager was redesigned, resulting in the second iteration, which enabled the cryoimager to have higher resolution. Figure 2.5 shows a sample grid image and a slice of a mouse eye sample provided by the cryoimager's second design demonstrating a

higher resolution obtained. In this implementation, the working distance between the tissue surface and the lens was reduced to 9.5 cm to get a stronger signal from the tissue. The lens was changed to a canon (EF 28-135mm, f/3.5-5.6 IS) standard zoom lens with less distortions, and higher resolution. In this design, since we need a lower distance between the tissue and the lens, a smaller filter wheel is used between the lens and camera that led to higher magnification. The emission filters for NADH is 445 nm (90 nm bandwidth, HQ 445/90M, Chroma, Bellows Falls, VT) and for FAD is 520 nm (35 nm bandwidth,FF01-520/35-25, Semrock, Rochester, NY). Finally, the camera used in this setting is a rolera (QImaging, EM-C^2 Rolera, Canada), which is featured with lower noise, high speed dynamic range, and more sensitive in terms of signal detection.

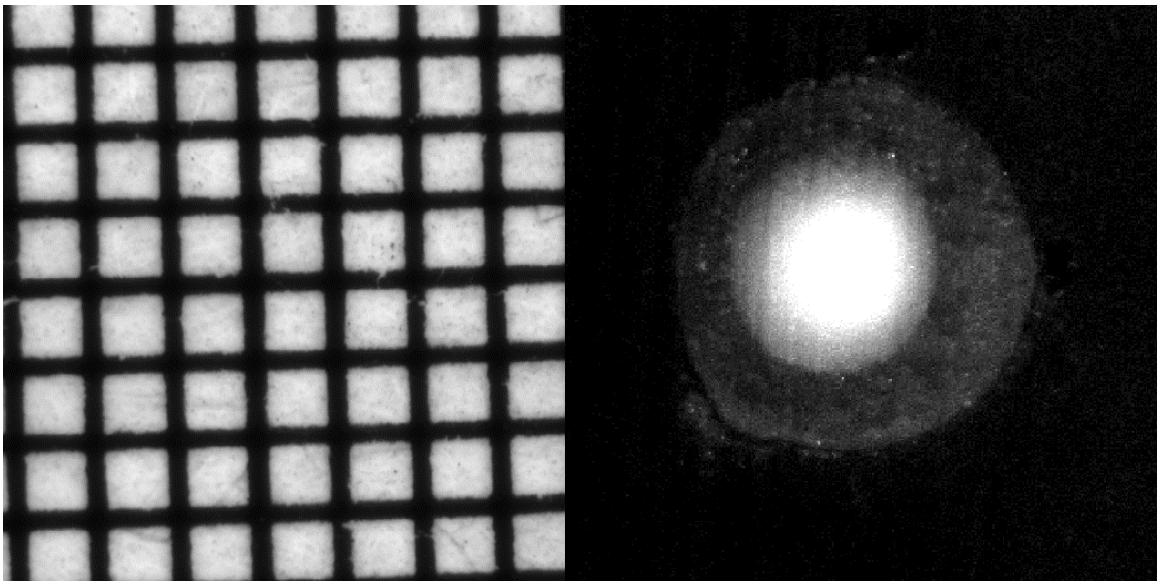

(a) (b)

Figure 2.5. Cryoimager's second design high resolution images (7mm× 8 mm). a) Grid b) A sample mouse eye image.

In this setting [79], after light is exposed on the tissue surface, the emitted fluorescent light first passes through a high resolution canon lens (Figure 2.6-1). The small emission filter wheel (Figure 2.6-2) is positioned right after the lens to band-pass filter the light at the desired emission wavelengths. Afterwards, an aqua CCD camera (Figure 2.6-3) records a fluorescence image of the tissue surface.

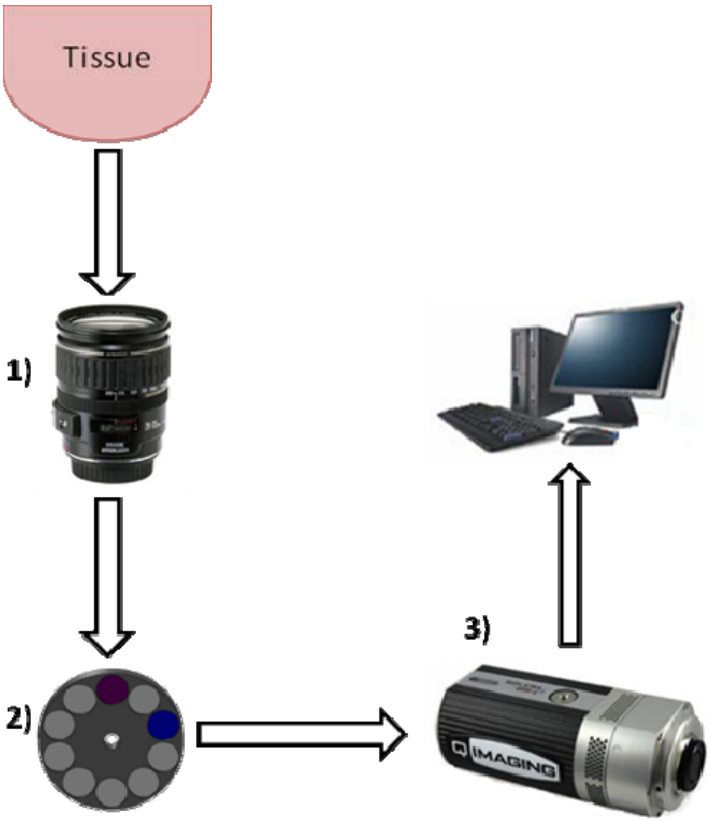

Figure 2.6. Cryoimager Detection. Block diagram of the components which make up the detection side of the cryoimager's second design. 1) Canon zoom lens. 2) Small emission filter wheel. 3) Rolera camera [79, 80].

Current Design

The third, and current, design of the device is a compromise between the first and the second design to obtain high resolution images while maintaining the field of view necessary for samples such as the mouse kidneys presented in this research. Figure 2.7 shows a sample grid image and a slice of a mouse kidney sample provided by the cryoimager's current setting. In the current setting, the combination of the big emission filter wheel from the first design, the high-resolution canon lens, and the Rolera camera from the second design are used. The working stage inside the device which the sample block is mounted on, is moving towards the lens. Thus, the working distance, i.e. the distance between the tissue surface and the lens is 24.3 cm, which is between the first and second design's distance. In this distance, the signal from the tissue surface is still strong and the field of view is large enough to image a whole kidney. This version of the cryoimager is suitable for imaging kidney samples since the kidneys are not as large as mouse lungs to need low resolution images and not as small as mouse eyes to need high resolution imaging.

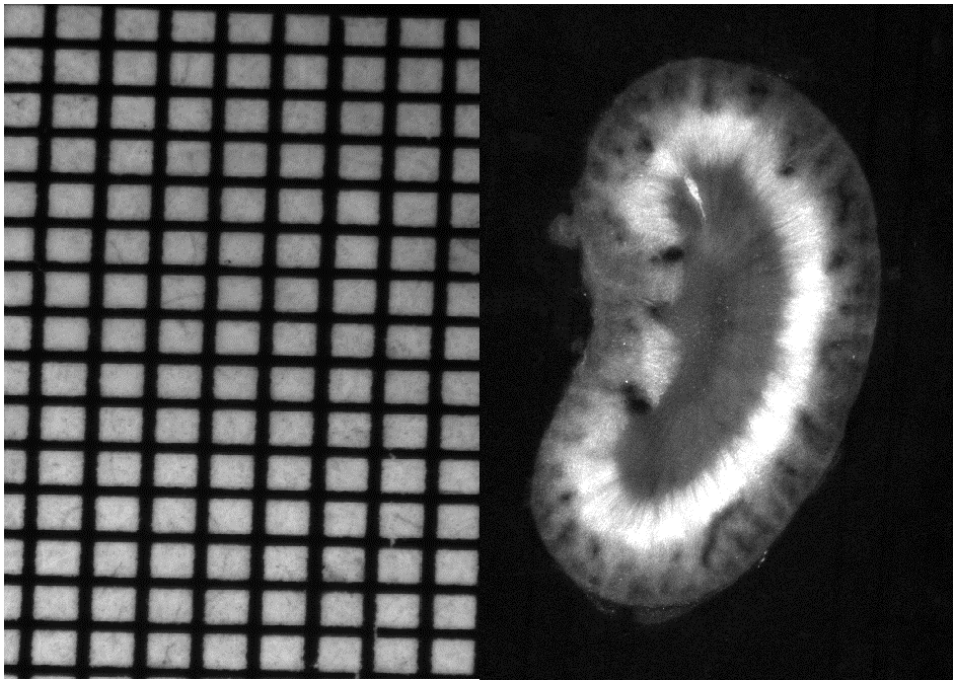

(a) (b)

Figure 2.7. Cryoimager's current design intermediate resolution images (9mm× 15 mm). a) Grid b) A sample mouse kidney image.

2.2.3. Entire System

A schematic summarizing the design of the cryoimager along with a picture of the actual system can be seen in Figure 2.8 and Figure 2.9. The light path begins with the mercury-arc lamp, where the light is guided to a cold mirror. The other side of the cold mirror is connected to an excitation filter wheel, where desired wavelengths of light are selected. This light is then delivered through a mirror to the tissue. The emitted fluorescent light from the tissue is then incident on the emission filter wheel as mentioned in the current design of the detection section.

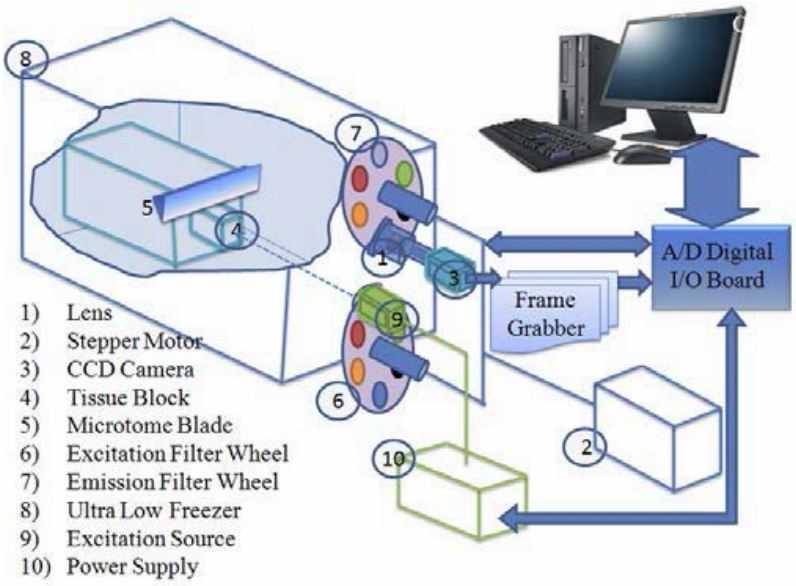

Figure 2.8. Cryoimager Schematic. Block diagram of the components which make up the cryoimager [49].

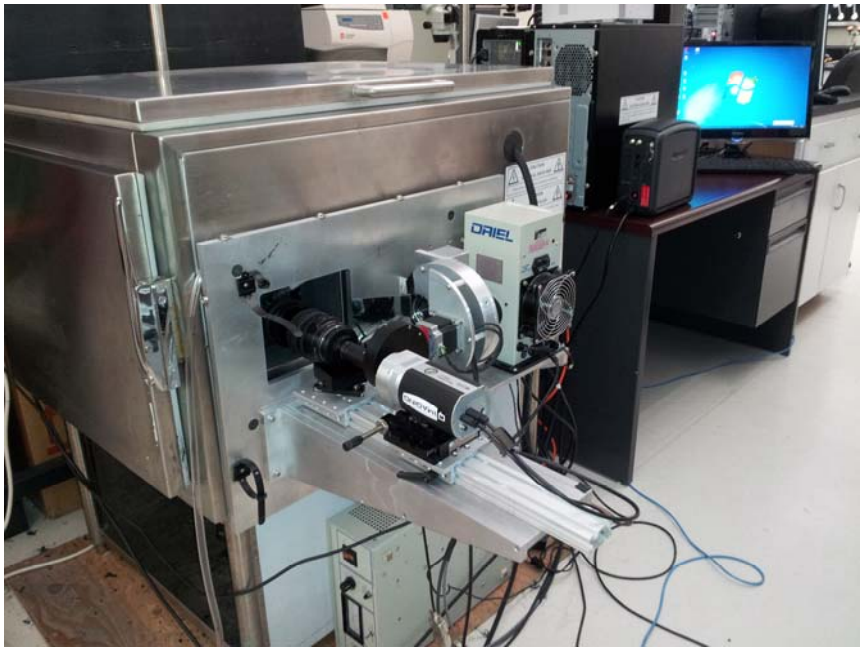

Figure 2.9. Cryoimager.

2.3. Hardware Components

2.3.1. Microtome Blade

The cryoimager contains a removable sharp blade that is positioned in the blade mount as can be seen in Figure 2.10 (a). The blade mount is then placed in the blade holder slot in the cryoimager and is powered by an AC motor (Blador, 1/3 HP AC motor VL 3501). The movement of the blade is controlled through a sensor that is located on top of the blade holder. Figure 2.10-b shows the sensor and the position of the blade inside the cryoimager.

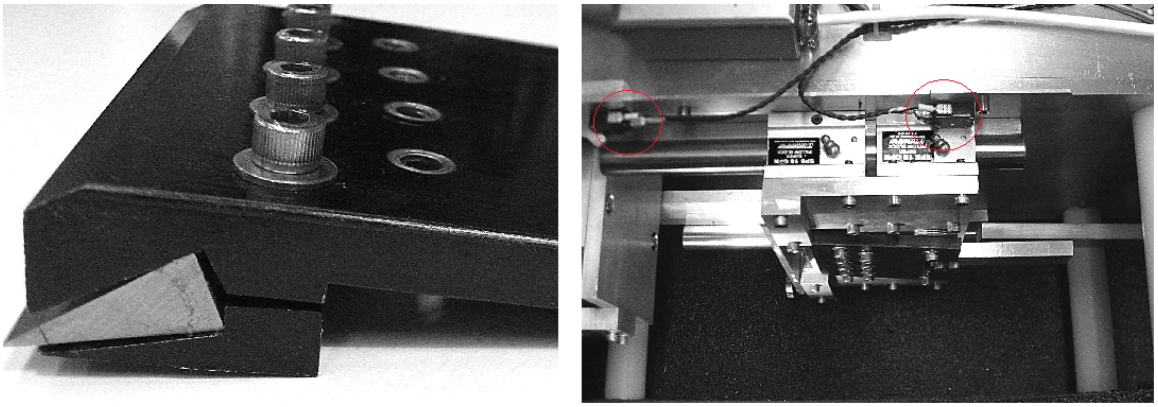

(a) (b)

Figure 2.10. Microtome blade. a) Blade mount. b) Blade and sensor's position inside the cryoimager.

2.3.2. Ultra-Low Freezer

The cryoimager includes an ultralow freezer, in which the inside temperature is controlled by an accurate interchangeable temperature sensor. To begin cooling the

sample chamber, the freezer should be plugged in and the control switch should be turned on. It takes 2-3 hours to cool down to the imaging temperature (-25^0c).

2.3.3. Filter Wheels

Two optical filter wheels rotate simultaneously to provide excitation/emission required for imaging fluorophores. Each of these filter wheels carries up to five different filters for simultaneous fluorophore imaging.

The excitation filter wheel is located in front of the mercurey-arclamp. A controller and a stepper motor (Oriental Motor Vexta Step Motor PK268-01B) with a step of 1.8 degrees moves the excitation filter wheel. This filter wheel could be dismounted for changing the filters.

The emission filter wheel is located between the glass viewing window and the camera. A controller and a stepper motor (Oriental Motor Vexta Step Motor PK268-01B) with a step of 1.8 degrees moves the filter wheel.

2.3.4. Camera

The CCD camera is located along with the glass viewing window and the lens. In the current design, the camera is mounted on a rail, which allows the forward, backward, and side-to-side movement easily. In this study, two different cameras were used, QImaging's EXi Aqua and Rolera EM-C^2. The Rolera is an EMCCD with high sensitivity and gain.

2.3.5. Lamp

The lamp used in this study is a 200 W mercury-arc lamp and the lamp module is located behind the excitation filter wheel. This type of lamp is of particular interest due to intense spectral peaks corresponding to the excitation peaks of both fluorophores of interest. Specifically, it has a peak at 365 nm that falls at the peak of the NADH excitation spectrum and a peak at 436 nm, which is at the peak of the FAD excitation spectrum as can be seen in Figure 2.11. After ignition, the lamp must remain lit at least 3 minutes to allow for warm-up and to reach its highest power.

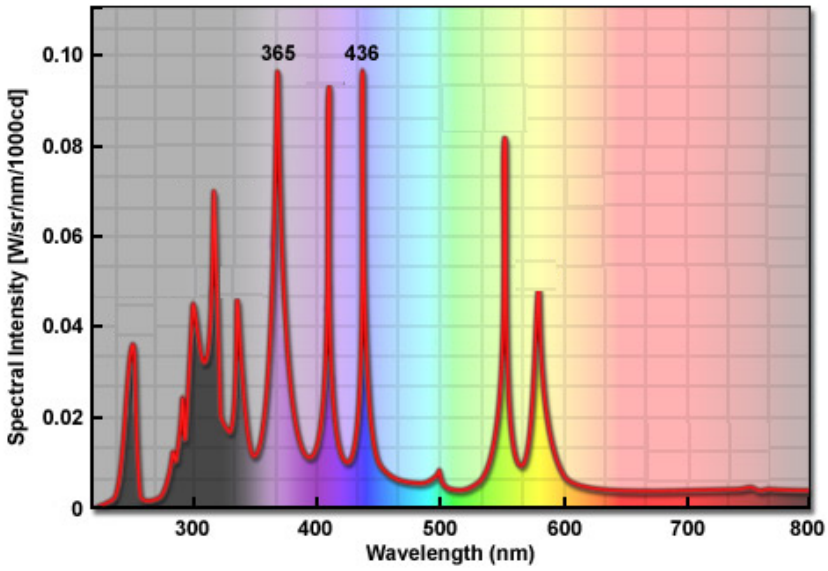

Figure 2.11. Spectral intensity of mercury-arc lamp [81].

2.4. Sample Preparation for Cryoimaging

There are several steps before the sample is ready for cryoimaging, including tissue preparation, sample freezing, mounting medium preparation, and sample embedding. These steps are explained in more detail in the following sections.

2.4.1. Tissue preparation

Ins2Akita heterozygous (Akita/+) male mice were obtained from Jackson Laboratories, where the colony is maintained by breeding C57BL/6J inbred females with Ins2Akita heterozygous males. Control animals were C57BL/6J male littermates. Only male mice were used in the experiments described below. All diabetic mice were left untreated. The Institutional Animal Care and Use Committee of the University of Wisconsin-Milwaukee approved all procedures. Genomic DNA was prepared from tail biopsies and the transgenic Akita/+ mice were identified by PCR screening using the following primers: 5′-TGCTGATGCCCTGGCC TGCT-3′ and 5′-TGG TCCCACATATGCACATG-3′. The amplified fragments were digested with FNU 4 HI, as recommended by Jackson Laboratories.

To generate Akita/+TSP1–/– mice, Akita/+ male mice were bred with TSP1–/– female mice. The resulting Akita/+TSP1+/– male mice were then bred with TSP1–/– female mice. Akita/+TSP1–/– male mice were determined by screening and the colony was maintained by breeding the respective male mice with TSP1–/– female mice. The litters were screened for Akita/+ and TSP1–/–.

2.4.2. Freezing protocol and storage

After the organs are experimentally prepared, the samples should be frozen through the following protocol. In order to preserve tissues metabolic state, flash freezing in liquid Nitrogen (LN_2) is used. Before putting the tissue in LN_2, first it is placed in the isopentane (2-methyl butane). A stainless steel or Pyrex container of isopentane is held in a Dewar flask, containing LN_2. Isopentane could be chilled in LN_2 (-176 C) for a smooth freezing. The isopentane will start to become opaque as it nears freezing. The isopentane should be chilled near to the end of the experiment when the tissue is ready to be frozen. The tissue is immersed in isopentane for 1-2 minutes. Then the tissue is removed from isopentane, and placed in LN_2. This method has the advantage of very rapid freezing without cracking due to sudden temperature change. For fluorescence imaging, we need to embed the tissue in specific mounting medium that is not fluorescent in excitation wavelengths of interest. Frozen tissues can be stored in a LN_2 dewar or an ultralow freezer (-80 C) to be imaged later.

2.4.3. Mounting medium preparation

The mounting medium is prepared in the Biophotonics lab (UWM), using Polyvinyl Alcohol (PVA, Grade 71-30, PVOH7130, Chemical Store Inc.,Clifton, NJ), distilled water and carbon black powder (Daniel Smith Dry Pigment, 284030040, Daniel Smith Inc., Seattle, WA). To make one liter of the embedding medium, 80 g of PVA is added to 920 g of boiling distilled water and stirred to make a homogeneous transparent

medium. Then the solution is cooled down and 80 g of carbon black is added and mixed thoroughly and refrigerated for 4-5 days before use.

2.4.4. Sample embedding in black mounting medium

The first step to embed a tissue sample is to prepare a chilled sample plate (Figure 2.12-a) and a teflon container (Figure 2.12-b), which sits on top of the plate (Figure 2.12-c). Prior to embedding the frozen tissue sample in a teflon container, a layer of black mounting medium 0.5 to 1 cm thick was frozen to the bottom of the container as the base.

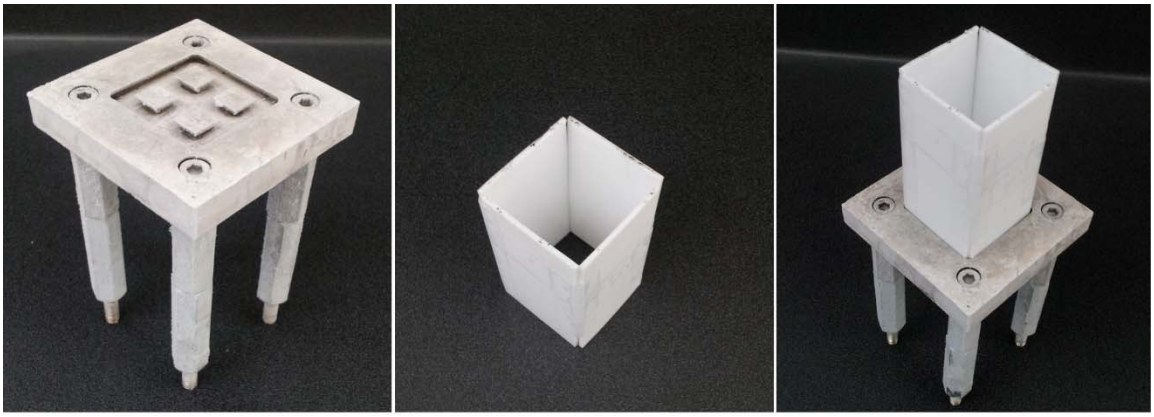

(a) (b) (c)

Figure 2.12. Sample embedding tools. a) Sample plate. b) Teflon container. c) Container on top of the plate.

The tissue sample is prepared by trimming any excess tissue, especially fat tissue that will fluoresce under certain filter combinations, and by rinsing off any frost with de-ionized water. The surface of the frozen mounting medium should be scored to provide grip for the fresh layer of the mounting medium and the sample, which is put on the surface. The sample is firmly placed on the puddle as can be seen in Figure 2.13(a) and

the container is filled with the black mounting medium until the sample is covered. This assures complete envelopment of the sample by the mounting medium. While pouring the mounting medium, bubbles should be avoided to maintain the image quality. After embedding the sample, the container is placed in the ultralow freezer for 8-10 hours before imaging. Figure 2.14(b) shows a sample block ready for cryoimaging.

(a) (b)

Figure 2.13. Sample embedding. a) Sample on the mounting medium. b) Sample block ready for cryoimaging.

2.4.5. Sample plate mounting in cryoimager

After the sample is securely frozen onto the plate, the sample plate is mounted on the sample carriage in the cryoimager using four nuts. Movement of the sample carriage stage is controlled through the computer using a controller and a stepper motor (Oriental Motor Vexta Step Motor PK268-01B) with step size of 1.8 degrees. The stage on which

the plate is mounted moves back through the software until it is exactly in front of the blade.

2.5. Imaging Software

To control all of the hardware movements, as well as record the images and display them while slicing is in progress, a LabVIEW program is written. Once the program starts, it checks the presence of the excitation and emission filter wheels, the sample setup motor, and the Q Imaging camera. The software controls the imaging through three primary panels: main, setup, and acquire. These three are responsible for all aspects of the program including showing the cooling status of the camera, changing the camera settings, setting up file location, positioning the filter wheel, positioning the sample and setting the slice thickness, adding a new filter set to the experimental setup, and controlling the automated image acquisition. In the following sections, the imaging software operation will be explained in more detail.

2.5.1. Camera cooling status

The main panel is the top-level instrument panel for the cryoimager program and includes a display of the current camera temperature and a cooling status, which indicates whether the camera has reached the regulated temperature lock. A snapshot of the main panel can be seen in Figure 2.14.

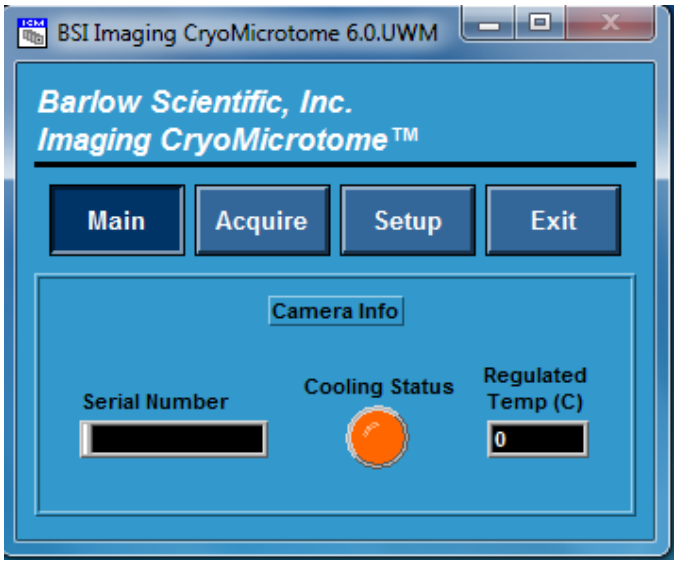

Figure 2.14. Main panel. Showing the cooling status of the camera.

2.5.2. Imaging setup

The setup panel is the gateway panel to control the majority of the cryoimager subsystem configuration. This panel enables the user to change the camera settings, introduce the file location, change the position of the filter wheel, move the sample inside the cryoimager and determine the slice thickness, and finally add a new filter set to the experimental setup. A snapshot of this panel with its subsystems can be seen in Figure 2.15.

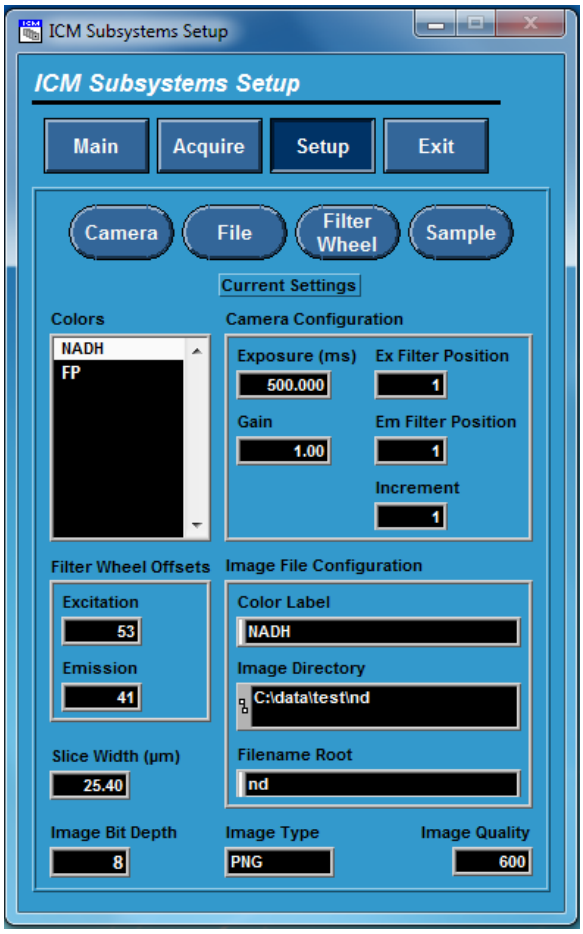

Figure 2.15. Setup panel. A snapshot of setup panel and its subpanels.

Camera configuration setup

The setup camera subpanel modifies the camera configuration for each filter set in the experiment. A live display of the sample is also shown to see the result of modifications applied to the camera configuration. A snapshot of the setup camera panel can be seen in Figure 2.16.

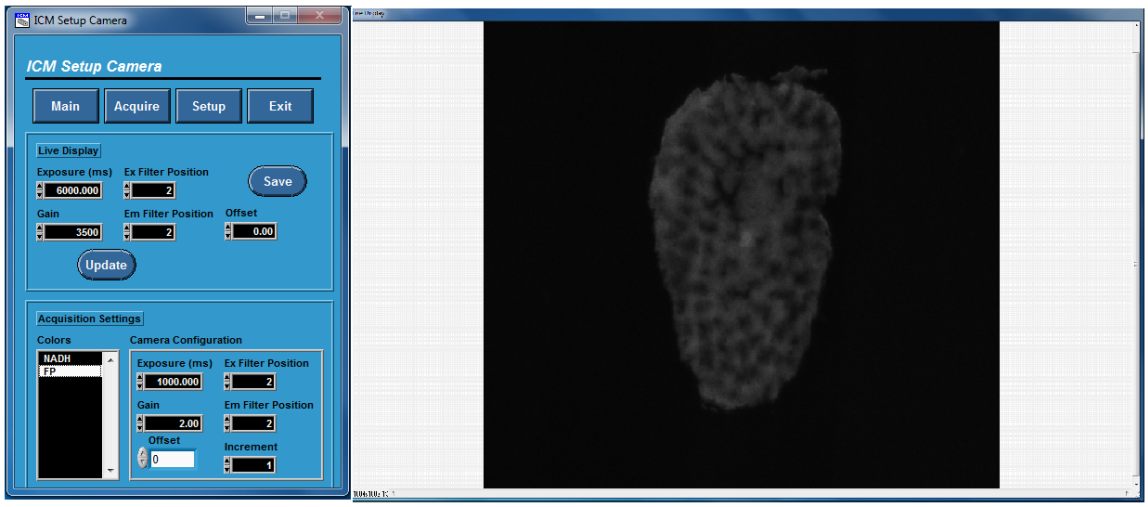

Figure 2.16. Setup camera subpanel. Modifying camera configurations.

The camera exposure time is set in intervals of 1 msec and the valid value range is from 1 msec to 59 minutes. The normalized camera gain could be set in the range of 0.804 to 34.7 for the Aqua Exi camera, whereas the electron-multiplying gain can be set from 0 to 4095 for the Rolera camera. The excitation and emission filters for each filter set can be controlled by entering their appropriate position number. The valid value range of both filters is 1 to 5. To control the frequency of imaging on each channel, in terms of the number of slices between imaging, the increment parameter can be used.

Image file setup

The setup image file subpanel modifies the image file destinations and configurations for each filter set in the experiment. New filter sets can be added or the existing filter set can be removed. Image file types supported by the software are BMP, JPEG, PNG, TIFF, and AIPD, of which PNG is chosen for our experiments, since it involves lossless compression. The amount of compression applied to the image files can

be defined as well. The valid value range is from 0 to 1000 and a higher value corresponds to less compression. In our experiments, the image quality is set to 600. Figure 2.17 shows a snapshot of the setup file subpanel.

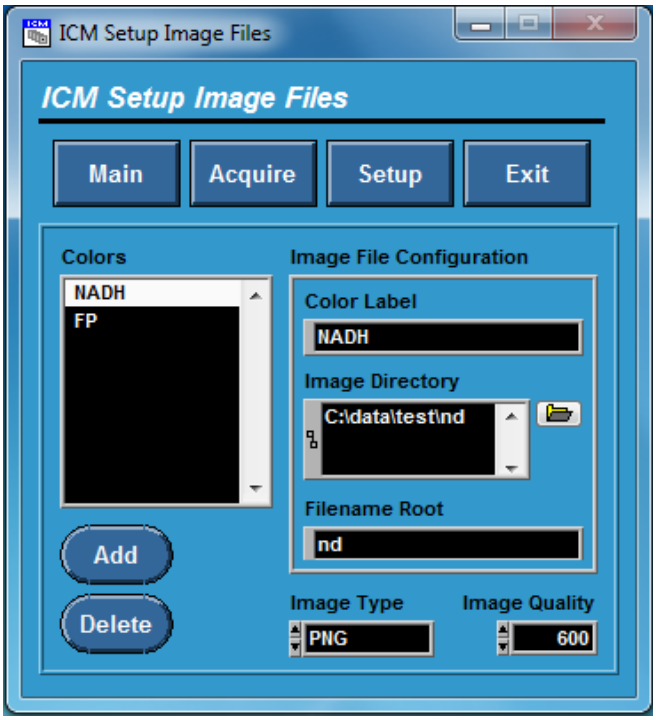

Figure 2.17. Setup image file subpanel. Modifying the image file destinations.

Filter wheel setup

The setup filter wheel subpanel calibrates both of the filter wheels by adjusting the zero sensor offsets. The excitation zero offset is the offset from the zero sensor position to the first filter position of the excitation wheel and it is set to 53 in our experiments. The emission zero offset is the offset from the zero sensor position to the first filter position of the emission wheel and it is set to 41 in our experiments. Figure 2.18 shows a snapshot of the filter wheel subpanel.

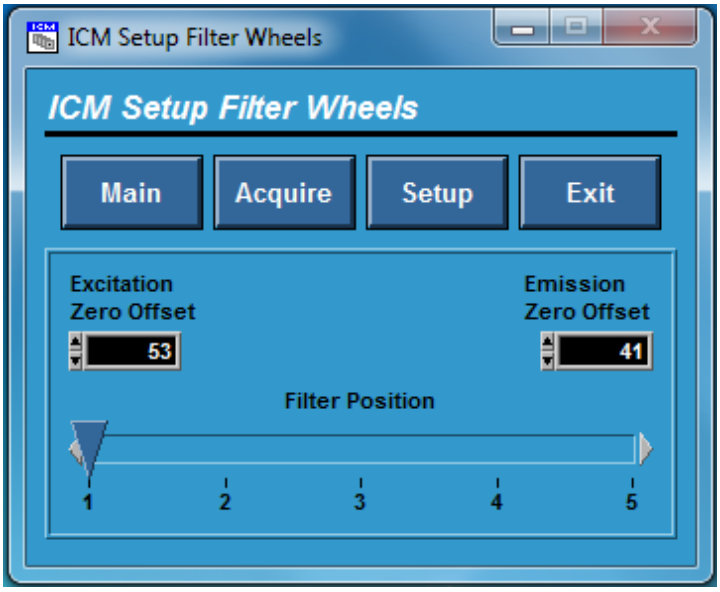

Figure 2.18. Setup filter wheels subpanel. calibrating the filter wheels.

Sample setup for cryoimaging

The setup sample subpanel positions the sample block and sets the sampling slice width. The travel direction of the sample translator can be set to move away from or towards the blade and a display shows the relative distance the sample has traveled in mm. The width of a single sample slice can be set between 1.59 µm to 1 cm. Figure 2.19 shows a snapshot of the setup sample subpanel.

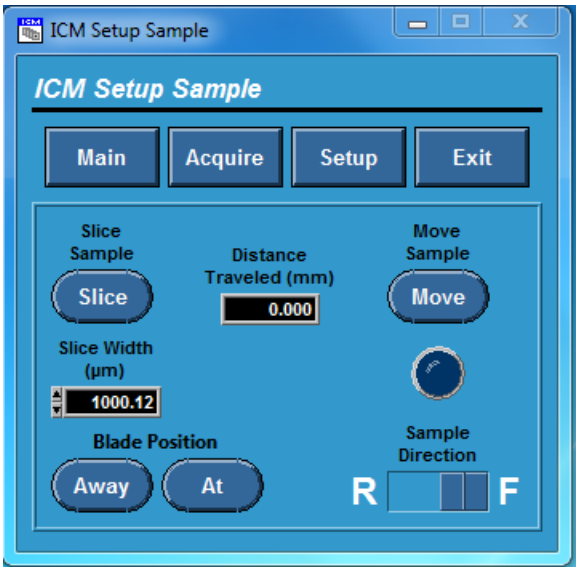

Figure 2.19. Setup sample subpanel. Positioning the sample block and setting the slice thickness**.**

2.5.3. Controlling the image acquisition

The automated image acquisition panel for the cryoimager experiments enables the user to start slicing the sample, and collecting images for each filter set in the experiment, as well as pausing or stoping the slicing and imaging after the current scan is completed. A snapshot of the image acquisition panel is shown in Figure 2.20.

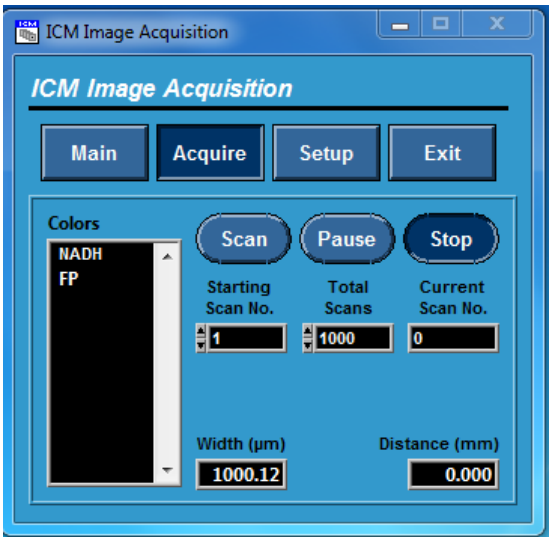

Figure 2.20. Image acquisition panel. Image acquisition control.

2.6. Sample Images from Cryoimager

Aqua camera captures color images with the pixel size of 6.45µm × 6.45 µm and total pixel number of 1392 × 1040 in an image. The digital output of this camera is 8 bits/14bits and the images captured by this camera have high resolution. Rolera camera captures images with the pixel size of 8 µm 8 × µm and total pixel number of 1004 × 1002 in an image. The digital output of this camera is 8 bits/14bits and the images captured by this camera have lower resolution compared to Aqua. Figure 2.21 shows a sample panel of NADH and FAD typical kidney images captured by Aqua camera.

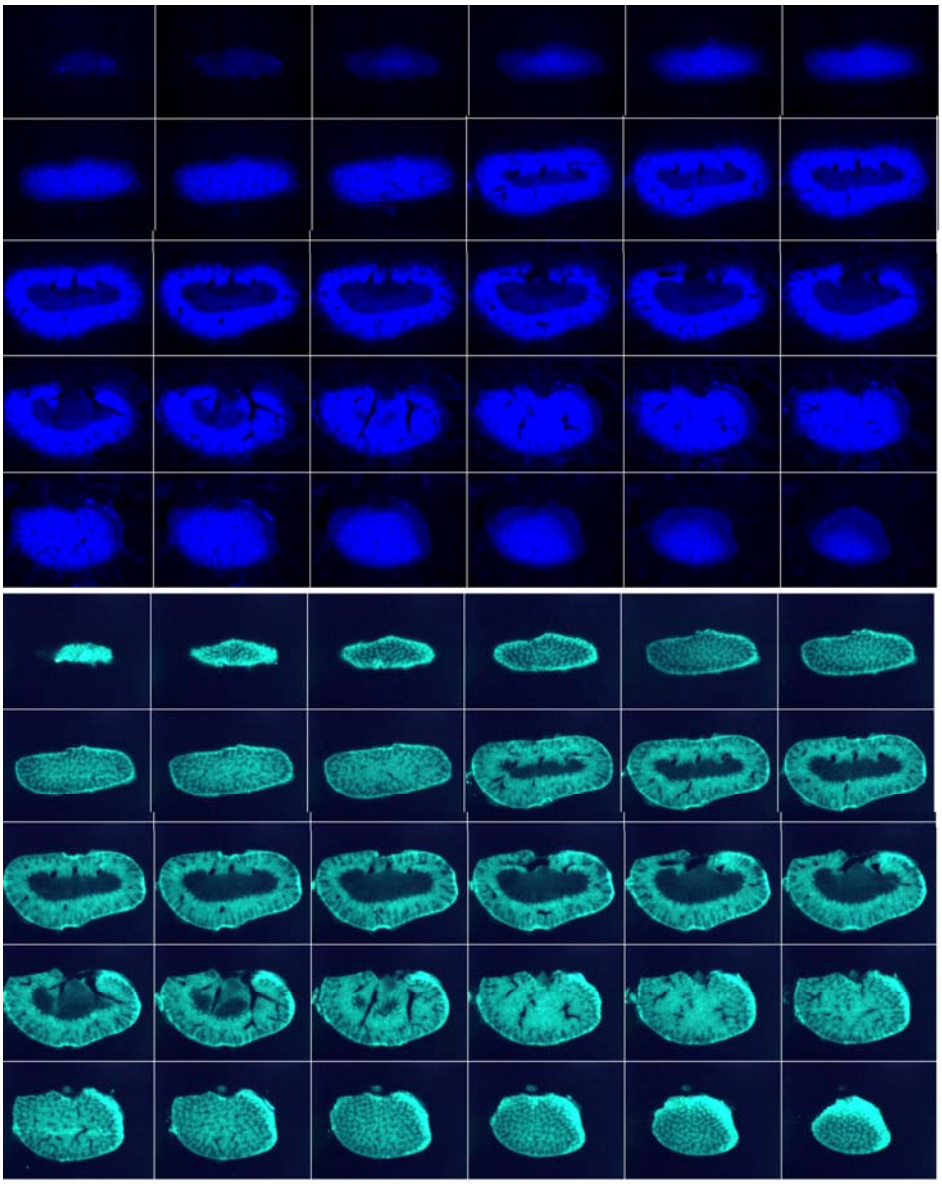

Figure 2.21. NADH and FAD kidney image panel. The top panel shows the NADH and bottom panel shows the FAD kidney images from cryoimager.

Chapter 3

Image Processing

3. Image Processing

3.1. Pre-processing in ImageJ

Before processing the images in MATLAB for results, the raw images are loaded in ImageJ for the examination of possible problems and correction. Based on the thickness in the Z axis chosen during imaging, each kidney sample result in 300 to 400 images in each of the NADH and FAD channels. All the images, each corresponding to a different depth, are then merged into a single file to construct NADH and FAD stacks using ImageJ.

3.1.1. Removing Undesired Slices

During tissue slicing, if the chosen slice thickness is very thin (around 10 to 15 μm), sometimes the tissue surface which was just sliced by the blade folds and attaches to the top of the sample block and destroys the next image and the next slide needs to be discarded. Figure 3.1 shows some sample slices in a stack of images in NADH channel which are removed in this step. Both image stacks of NADH and FAD are searched for removal of these unwanted slices. The removal of these undesired slices helps in producing more accurate results and better image representation.

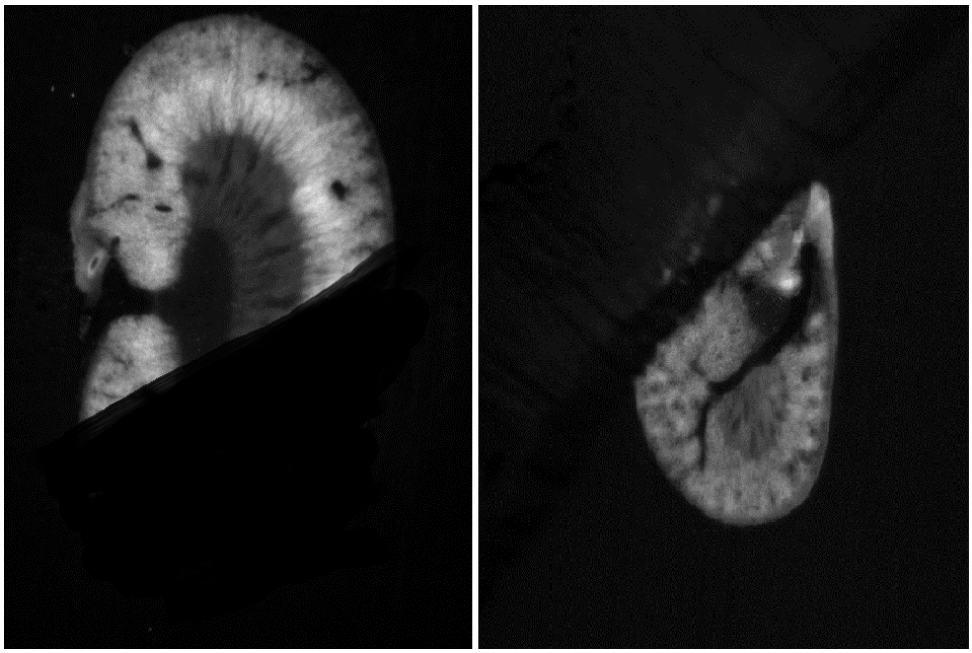

Figure 3.1. NADH stacks of images. Sample undesired slices in an imaging experiment.

3.1.2. Checking for Intensity and Exposure Changes

The NADH and FAD image stacks are then checked for any sudden increase or decrease in intensity in the middle of an experiment, which could have been caused by the user to prevent saturation or improve the contrast. Figure 3.2 shows two consecutive slices in an imaging experiment, in which the exposure time was increased by the user to increase tissue intensity and as a result the contrast during imaging. While processing, the images compensate for the intensity changes using a linear scaling factor with the background as they intercept.

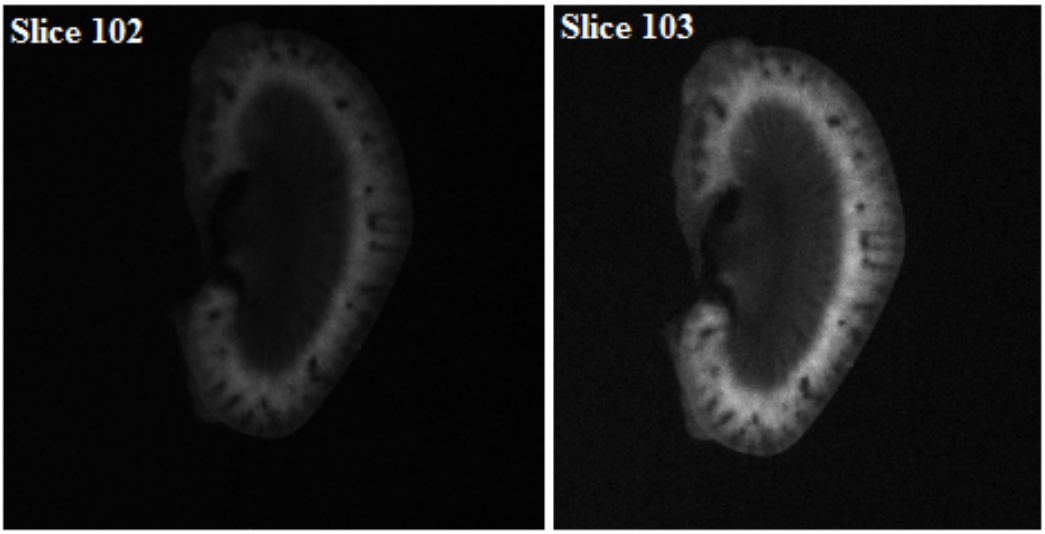

Figure 3.2. Intensity change in an experiment. Two consecutive NADH images showing an increase in the intensity in an experiment .

3.1.3. Checking for Camera Movement

In some experiments, the camera has a slight movement during slicing and imaging due to the blade's movement. Figure 3.3 shows the first and the 100th slice in an experiment, in which the toothpicks embedded on either side of the sample, where the camera movement caused a shift of the image during slicing. The camera movement is caused by the blade continuously cutting through the sample block, and each cut induces a slight vibration in the stage, to which the camera and lens are mounted. This undesired movement can be avoided as in the case in later experiments, by tightening the camera and lens to the stage, and securing the lens of the camera in place.

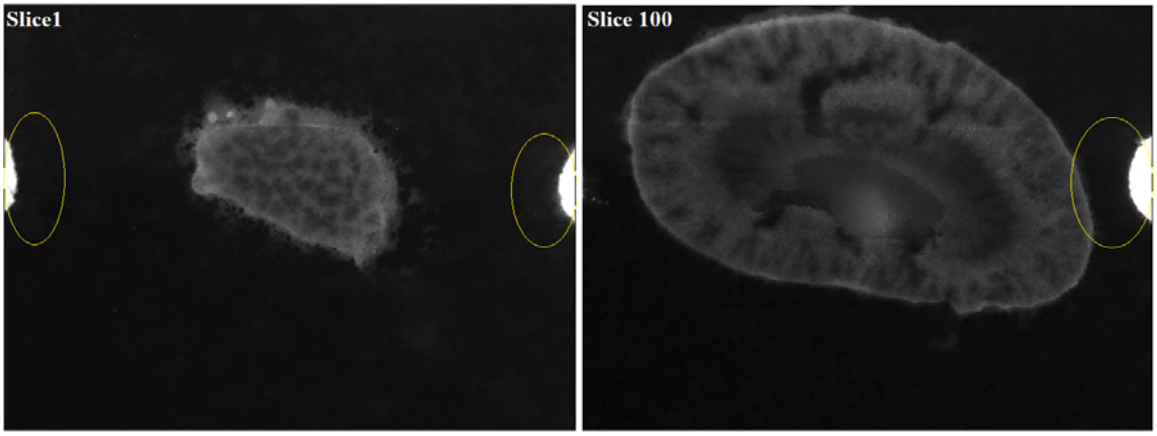

Figure 3.3. Camera movement. The first and the last slice in an imaging experiment showing the camera movement based on the toothpick's position.

3.1.4. 3-D Reconstruction to check

To check if all parts of the sample were imaged correctly and completely, a 3-D structure is reconstructed from the raw images. If, for any reason, some part of the sample is broken or missed, it can be seen in the 3-D structure. Figure 3.4 shows the 3-D reconstructions of a whole and halfway cut kidney, which were imaged properly.

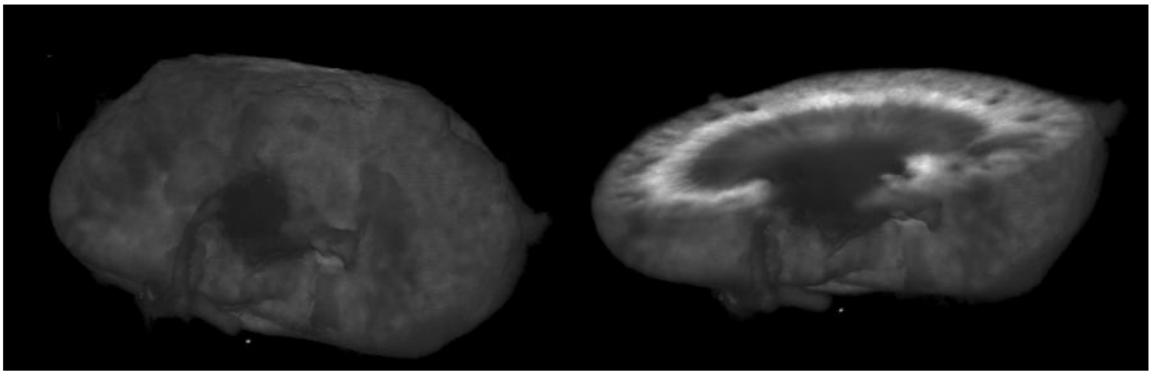

Figure 3.4. Kidney 3-D reconstruction from raw images. Whole and half way cut kidney.

3.1.5. Imaging Calibration

A calibration method was designed to compensate for day-to-day variations of light intensity and non-uniformity of the illumination pattern. Figure 3.5 shows all the calibration images, which are taken at the beginning of each experiment and before slicing the tissue. In the first row on the right an image of the grid is shown, which is used to set the focus of the camera before imaging and acquiring the resolution of imaging. On the right, a sample dark current image is shown. This image is used for background subtraction.

The second row shows the images of a phantom captured in NADH and FAD (left to right) channels in the same field of view. The phantom was placed in the same position as tissue and imaged in all channels. These phantom images are used to correct for day-to-day light intensity variations and other experimental changes.

The third row shows the flat-field images in NADH and FAD (left to right) channels. The flat-field image is captured from a uniformly fluorescent and flat object. Since the fluorescence of the standard is in both the NADH and FAD channels, it also accounts for day-to-day light intensity variations as well as possible non-uniform distribution of light on the sample. All the images in each channel were then normalized by dividing each image to the flat-field image, captured in the same channel.

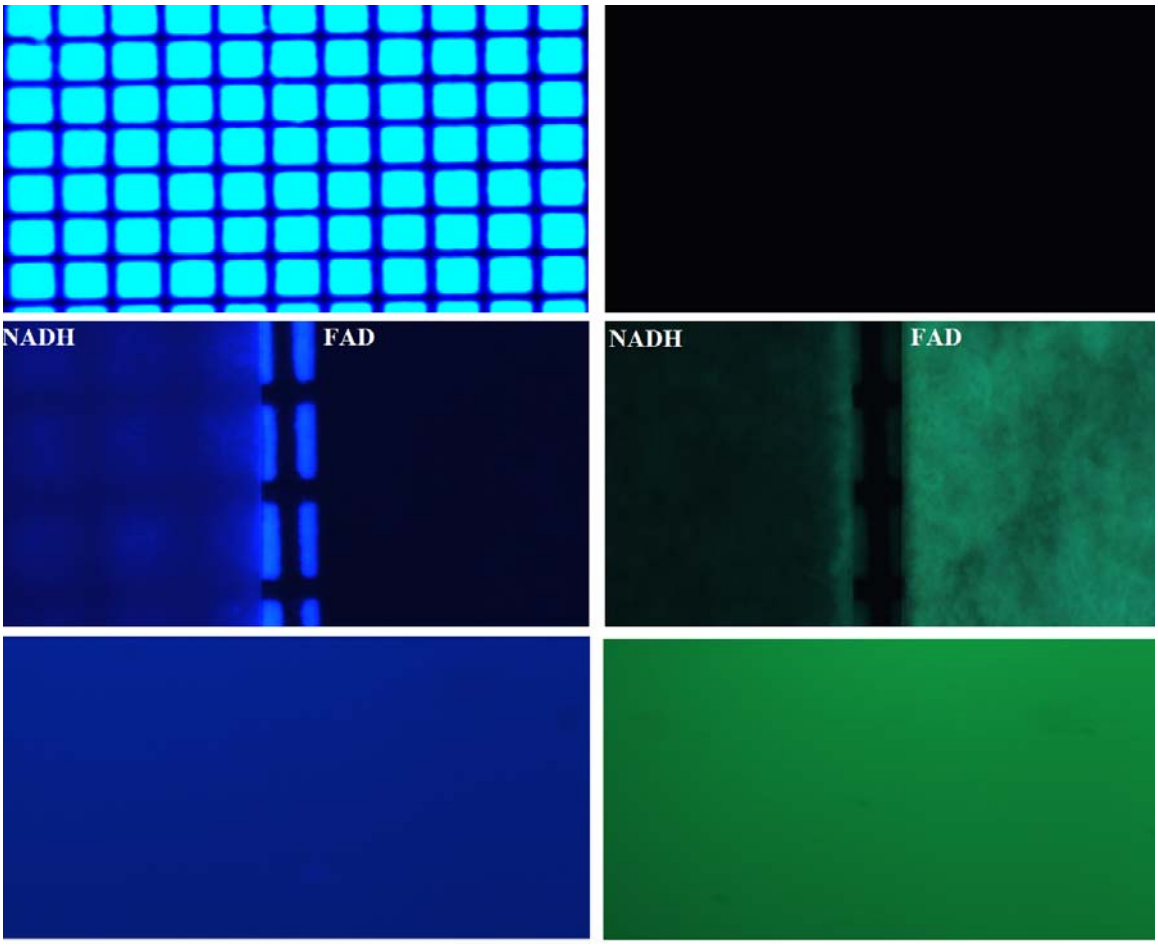

Figure 3.5. Calibration Images. The first row shows the grid and the dark current image (left to right). The second row shows the phantom images taken in NADH and FAD channels, respectively. The third row shows the flat-field images in NADH and FAD channels from left to right

3.2. Redox Calculations and Data Representation

3.2.1. Reading NADH and FAD Images in MATLAB

After pre-processing, FAD and NADH autofluorescence images (containing 300-400 slices per kidney) from each group of kidneys were loaded in MATLAB (The MathWorks, Inc., Natick, MA). The images are then pseudo-colored using the jet colormap for ease of visualization and background subtraction. Figure 3.6 shows a

sample pseudo-colored image from each of the NADH and FAD channels with the jet colormap. After background correction and exposure compensation, NADH fluorescence images are divided by the corresponding FAD images to calculate the NADH redox for each slice of a kidney sample and to construct the redox stack. Final redox presentation is then possible through one of the following methods, depending on the organ and desired part of the tissue.

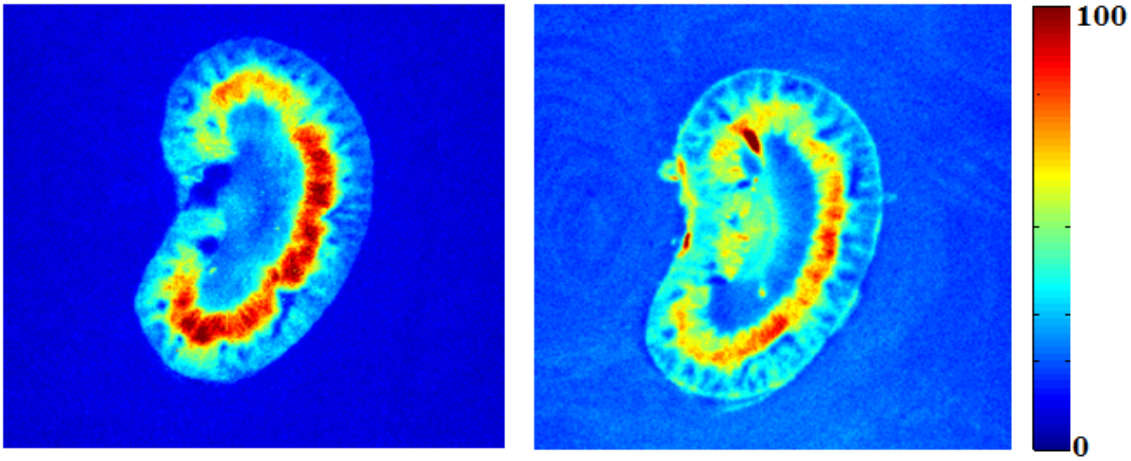

Figure 3.6. Pseudo colored NADH and FAD images. One representative image in each set is used for background correction.

3.2.2. Representation of Data

One Slice Representation

In this method, one representative slice from the whole sample is chosen to display the results. Figure 3.7 shows NADH, FAD, and NADH redox images from one slice of a wild type (WT) mouse kidney, which shows one cross-section of the tissue.

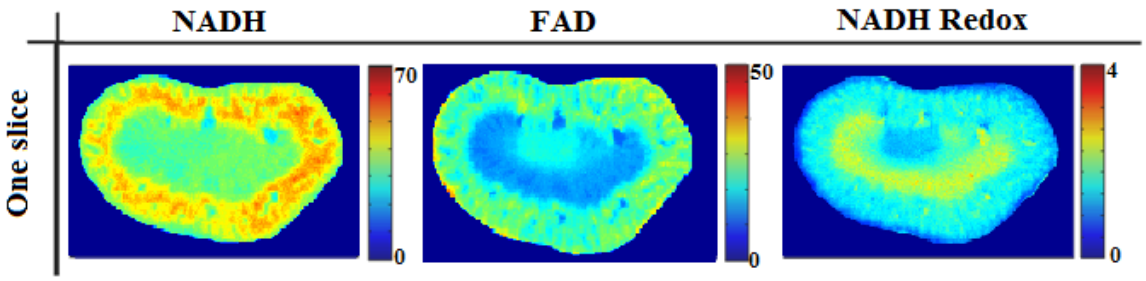

Figure 3.7. One Slice Method. NADH, FAD, and NADH redox images of a WT kidney.

Whole Volume Representation

In this method, the composite images that were created using all slices in NADH, FAD, and redox are used. These 3-D composite images are used for representation and comparison of the data and calculation of the histograms. Figure 3.8 shows the rendered NADH and FAD images and the redox volume calculations of a WT kidney.

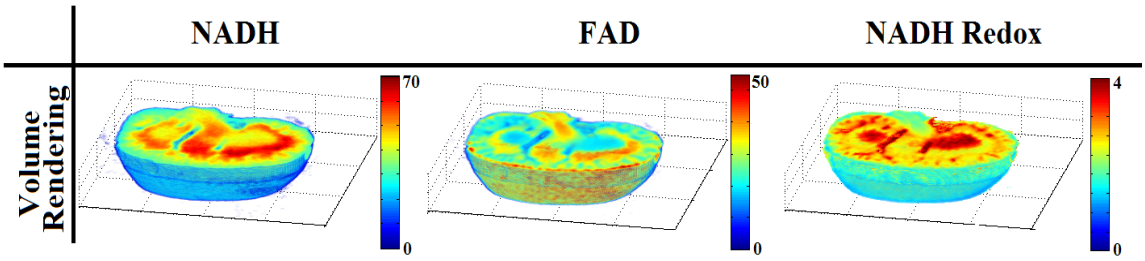

Figure 3.8. Whole Volume Method. NADH, FAD, and NADH redox volume images of a WT kidney.

Maximum Projection Representation

In this method, the maximum intensities along the z axis of the composite images (3-D volume in NADH, FAD, and redox ratio) were calculated and used for representation and comparison of the data. Figure 3.9 shows the maximum projection of NADH, FAD, and NADH redox in a WT kidney.

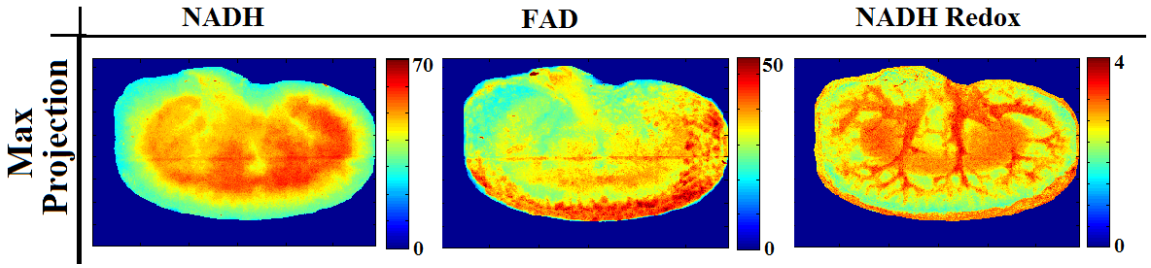

Figure 3.9. Maximum Projection Method. NADH, FAD, and NADH redox maximum projected images of a WT kidney.

Discussion on Three Representation Methods

The aforementioned three methods have their own advantages and disadvantages. The drawback of presenting the results using one slice is the sampling error in which the result is only dependent on one slice and may not accurately present the whole tissue's redox state. However, it has the advantage of emphasizing a specific part of the tissue, which is of more interest. In addition, this method is the least computationally intensive of the three.

The advantage of the whole volume method is that every single voxel of the images is used in redox calculations. This is beneficial in some tissues, such as lung and liver, which have almost a homogeneous tissue and the majority of the tissue is of our interest in redox calculation. However, in other tissues such as kidney, analysis of the entire 3-D volume includes a large portion of tissue, which is not the focus of this research.

The maximum projection method is advantageous in that it may reveal details, which are hidden in the other methods. The kidney is an example in which, the tissue shows vascular dysfunction and a higher fluorescence intensity caused by OS during the course of diabetes. As a result, application of the maximum projection method emphasizes the differences in the components, which does not include the majority of the tissue.

Figure 3.10 shows a bcl-2 kidney panel with all three methods for representation of the results. Bcl-2 plays an essential role during kidney development and a lack of bcl-2 enhances apoptosis affecting kidney development and growth. It is proven for the bcl-2 deficient (bcl-2 -/-) mice kidneys to have a more oxidized biochemical state and a lower

redox ratio as compared to bcl-2 +/+ mice kidneys. Row one and two in Figure 3.10 shows the max projected images of bcl-2 +/+ and bcl-2-/-. The histogram on the right shows the fluorescence intensity distribution of all kidney images in both groups. The histogram shows a 56% change in the mean NADH RR in kidneys from the bcl-2 -/- group compared to bcl-2 +/+. Row three and four show the pseudo-colored images of one specific slice of the kidney tissue and the histograms on the right show the intensity distribution of that specific slice. As can be seen from the histograms, the change in the mean NADH RR is about 38% between bcl-2 +/+ and bcl-2 -/-, which is less than the first method. Row five and six show the whole volume of the kidneys from bcl-2 -/- and bcl-2 +/+ groups and their related volume histograms on the right. The histograms show a 38% change in the mean NADH RR of the whole kidney volume between the two groups, which is less than the changes in the maximum projection method. The changes are less in this method since the entire 3-D tissue volume is considered in the redox calculations.

As can be seen from the histograms of all three methods, the percentage change in the mean NADH redox is higher in the first method. Thus, the first method is more sensitive in terms of expected results. OS plays an early role in the development of vascular dysfunction associated with diabetic nephropathy and by using the maximum projection method, we can determine where this OS is occurring in the renal vasculature, namely the central region in the kidney tissue.

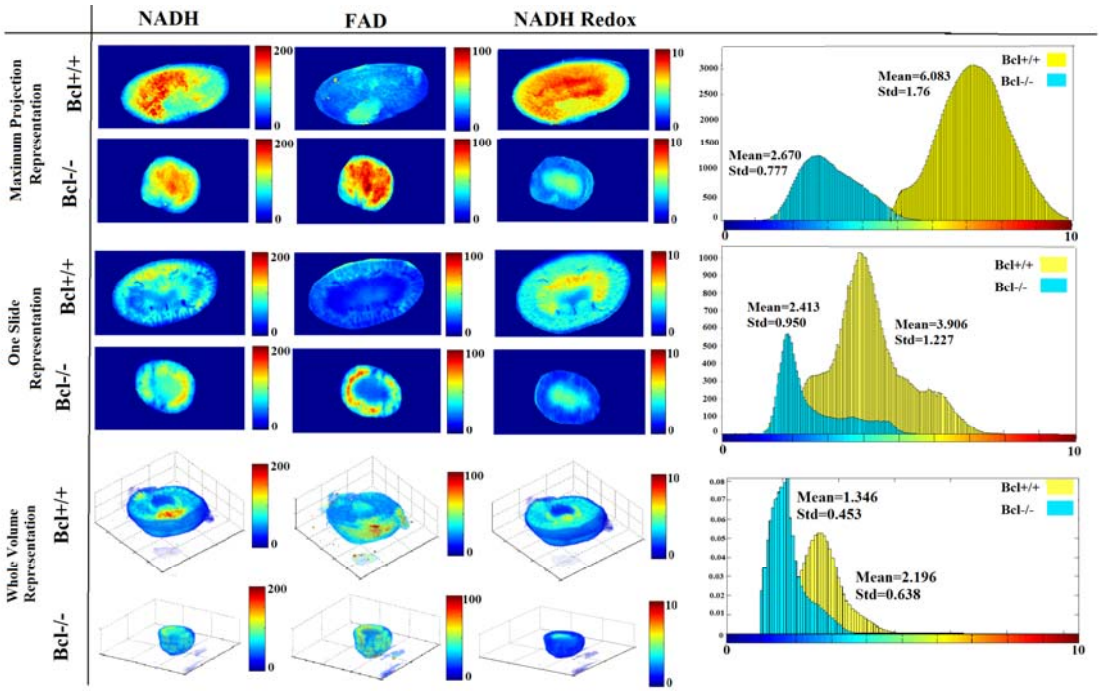

Figure 3.10. Bcl-2 Panel for Three Representation Methods. The first two rows show the max projection of NADH, FAD, and NADH redox (left to right) using all the fluorescence images. The second two rows show the pseudo-colored images from one kidney slice. The third two rows show the NADH, FAD, and NADH redox of whole kidney volume. The histograms for each method, which are located on the right side, show the maximum change in the mean NADH RR in the maximum projection method.

3.3. Statistical Analysis

Statistical analysis was also carried out for each group of kidneys using a one-tailed student's *t*-test with $P < 0.001$ as the criterion for statistical significance.

Chapter 4

Fluorescence Imaging Results

4. Results

4.1. Introduction

Diabetes, a common metabolic disorder, can trigger excess generation of ROS and plays an important role in increasing OS in various tissues, including the kidney. The increased OS during diabetes exacerbates the progression of disease and its associated complications. However, the temporal and spatial aspects of these changes and, more specifically, the time of onset of OS during diabetes remain unknown.

In this research, six categories of mice with different genotypes were studied, as follows. First, bcl-2 -/- mice, which are more sensitive to OS and thus are expected to have a lower NADH RR, were compared with their bcl-2 +/+ controls to verify the ability of the system to detect differences in OS. Next, Akita/+ and their WT controls were studied to determine whether a change in OS is correlated with the presence of diabetes. Similar to bcl-2 -/-, Akita/+ mice are more susceptible to OS and are thus expected to have a lower NADH RR. Finally, Akita/+TSP1-/- mice were compared with their control, TSP1 -/-, in order to evaluate the severity of diabetic nephropathy in these mice using the mitochondrial oxidative state as a quantitative marker. It should be noted that the name of each group indicates the only modification to the mouse, and thus Akita/+, Akita/+ TSP1 -/- and TSP1 -/- are not bcl-2 deficient.

4.2. Bcl-2

To ensure that cryogenic fluorescence redox imaging can effectively measure increased OS in kidney sections, the NADH RR was initially examined in kidney sections of wild type (bcl-2 +/+) and bcl-2-deficient (bcl-2 -/-) mice.

Bcl-2 plays an essential role during kidney development and lack of bcl-2 enhances apoptosis affecting kidney development and growth, and thus is of direct interest for this study. Absence of Bcl-2 causes a more oxidized state in tissue and, as such, the mitochondria are more oxidized in bcl-2 -/- mice as compared with their controls.

The cryogenic fluorescence imaging method was used on kidneys from 3 weeks-old bcl-2 +/+ and bcl-2 -/- mice. Figure 4.1 shows the max projected images of NADH, FAD, and NADH RR in bcl-2 +/+ and bcl-2 -/- mice kidneys. The NADH RR indicates a more reduced biochemical state in kidneys from bcl-2 +/+ mice with a mean value of 5.639 compared with a much smaller mean value of 2.004 in kidneys from bcl-2 -/- mice. Thus, kidney sections from bcl-2 -/- mice consistently demonstrated increased OS as expected, and are shown in Figure 4.1 with a decreased NADH RR, confirming the usefulness of this method for measuring OS.

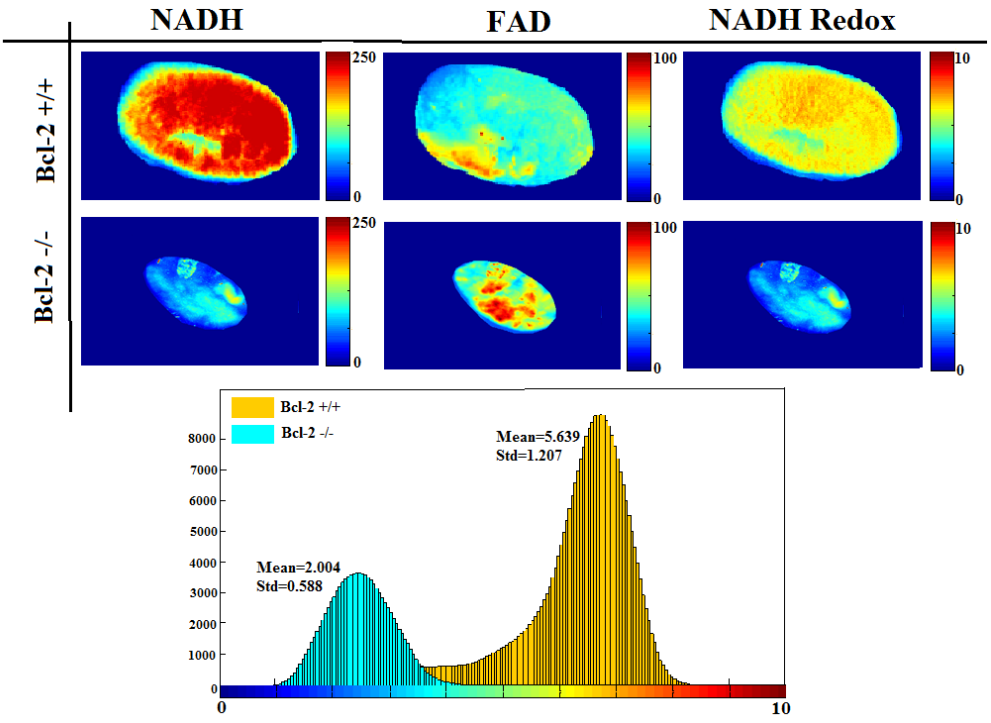

Figure 4.1. Representative 3 weeks old bcl-2 kidney panel. Representative max projected images of NADH, FAD and RR and their histograms in kidneys from 3 weeks old bcl-2 +/+ and bcl-2 -/- mice.

Bcl-2 is a known modulator of mitochondrial OS and its absence is associated with an increased OS state. The NADH RR showed a significant decrease in kidneys from bcl-2-/- mice as compared with their wild-type counterpart. The difference in mean values of the histograms in Figure 4.1 suggests that OS shifts the metabolic levels of cells.

4.3. Akita/+ Diabetic Mouse Model and its Control WT

Akita/+ mice develop type 1 diabetes as early as 4 weeks of age. Akita/+ and their WT controls in different diabetic stages (different ages) were studied to determine the onset and progression of OS during diabetes. Akita/+ mice are more susceptible to OS and are thus expected to have a lower NADH RR compared to their WT in the same age. Figure 4.2 shows the pseudo-colored representations of the maximum projection NADH, FAD and NADH RR images and histograms of the NADH RR for kidneys from 4, 8, 12, and 34 weeks-old WT and Akita/+. As can be seen from the max projected images and the histogram, the NADH RR does not show a significant difference in Akita/+ kidneys compared to its WT for 4 weeks-old kidneys, indicating that this age corresponds to the onset of diabetes. As the kidneys age, the histograms and max projected images show a significant decrease in the mean NADH RR of kidneys from 8, 12, and 34 weeks-old diabetic mice compared with their WT counterparts. The difference in the mean NADH RR becomes more significant in Akita/+ compared to WT by age and due to progression of OS as shown by separation of histograms. The histograms shows less than 10% change in the mean NADH RR in kidneys from 4 weeks-old diabetic compared to its WT. This change increases to 15% for 8 weeks-old kidneys, 28% for 12 weeks-old kidney, and 33% for 34 weeks-old kidneys. The increasing effect of OS on the kidney mitochondrial redox state as evaluated by a decrease in NADH RR can be seen in the histograms of Figure 4.2.

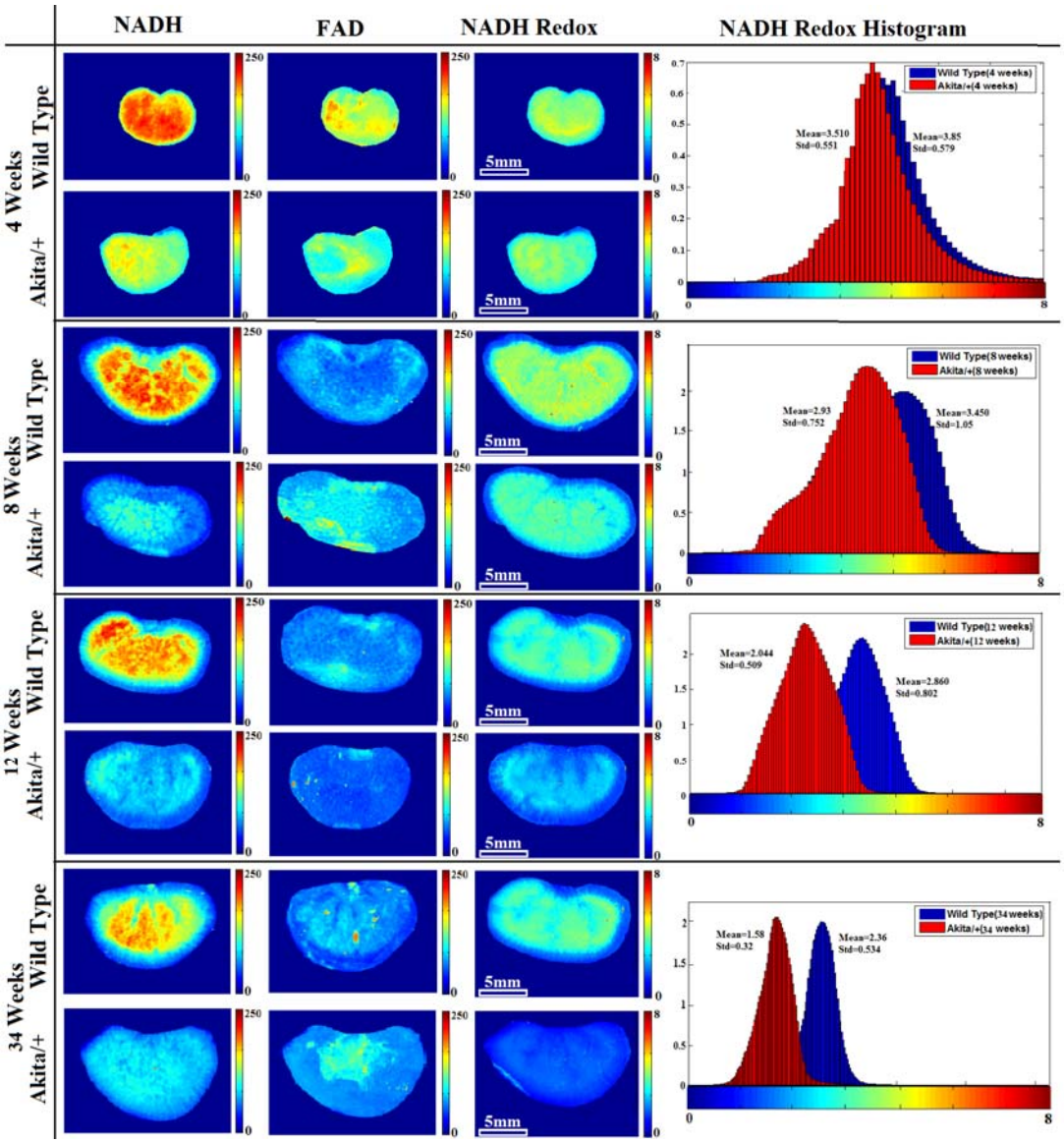

Figure 4.2. Representative Akita/+ and WT kidney panel. Representative max projected NADH, FAD and NADH RR images and their related histograms for kidneys from Akita/+ and mice and their controls in different ages.

To show the effect of age and OS in diabetic mice models, Akita/+ mice of different ages were investigated separately. Figure 4.3 shows the max projected images of NADH, FAD, and NADH RR as well as the NADH RR histograms of kidneys from 4, 8, 12, and 34 weeks-old Akita/+ mice. The NADH RR shows a visible decrease in kidneys

from 4 weeks-old diabetic mice compared with 8 and 12 weeks-old kidneys, which becomes more significant in kidneys from 34 weeks-old diabetic mice. The histograms in Figure 4.3 show a 20% change in the mean NADH RR of 4 weeks-old kidney compared to 8 weeks-old. This change increase to 44% and 60% for 4 weeks-old kidney compared to 12 and 34 weeks-old kidneys. Thus, these results show an increase in kidney OS with a longer duration of diabetes.

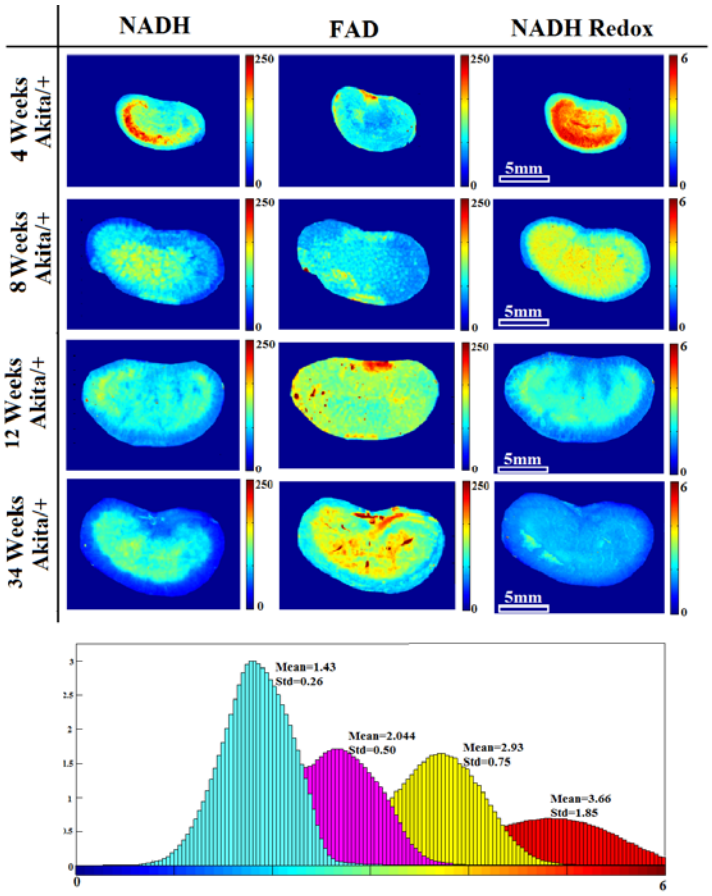

Figure 4.3. Representative Akita/+ kidney panel over age. Representative max projected NADH, FAD and NADH RR images and their related histograms for kidneys from 4, 8, 12, and 34week-old Akita/+ kidneys.

4.4. Akita/+TSP1-/- a More Severe Diabetic Model

The Akita/+TSP1-/- mouse is a novel diabetes model that exhibits severe nephropathy with a relatively short duration of diabetes compared with the parental Akita/+ mice. Thus, the mice that carry the Akita mutation and lack TSP1 (TSP1 -/-) serve as a model for severe diabetic nephropathy. Here the impact of the combination of these genetic modifications has been investigated on the mitochondrial redox state associated with the onset and progression of diabetes. To verify that the TSP1-/- genotype itself does not contribute to a more oxidized mitochondria, TSP1-/- has been compared with Akita/+ TSP1 -/- mice.

Figure 4.4 shows the pseudo-colored representations of the maximum projection NADH, FAD and NADH RR images and histograms of the NADH RR for kidneys from 3, 4, and 24 weeks-old Akita/+TSP1-/- and their related controls TSP1-/-. As can be seen from the NADH RR histogram for the 3 weeks-old kidneys, Akita/+TSP1-/- and its related control are not significantly different in mean NADH RR at this age, indicating that the symptoms of diabetes are not yet evident. The histograms show 10% change in the mean NADH RR in kidneys from 3 weeks-old AK/+TSP1-/- compared to its control. This change increases to 33% for 4 weeks-old kidneys, and 44% for 24 weeks-old kidneys. The results presented in the histograms indicate that the mean NADH RR of kidney from 4 and 24 weeks-old Akita/+TSP1-/- mice show a more significant decrease compared with their control mice, TSP1-/-, which is a direct result of more OS and complications due to severe diabetes.

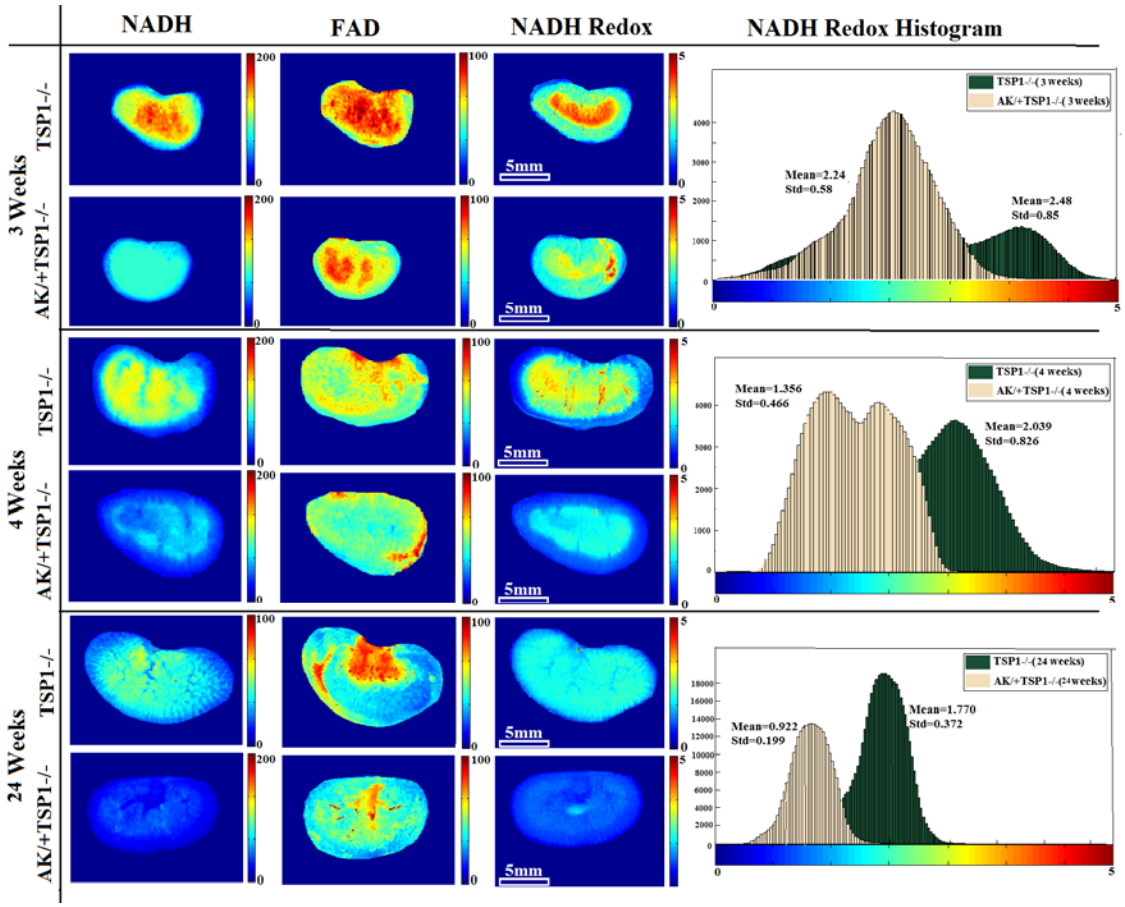

Figure 4.4. Representative Akita/+TSP1-/- and TSP1-/- kidney panel. Representative max projected NADH, FAD and NADH RR images and their related histograms for kidneys from 3,4, and 24 weeks-old Akita/+TSP1-/- and related controls.

To show the effect of OS progression with age in severe diabetic mice models, Akita/+TSP1-/- mice of different ages were investigated separately. Figure 4.5 shows the max projected images of NADH, FAD, and NADH RR as well as the NADH RR histograms of kidneys for 3, 4, and 24 weeks-old Akita/+TSP1-/- mice. The NADH RR shows a visible decrease in kidneys from 3 weeks-old diabetic mice compared with 4 weeks-old kidneys, which becomes more significant in comparison to the kidneys from 24 weeks-old diabetic mice. The histograms in Figure 4.5 show a 40% change in the

mean NADH RR of 3 weeks-old kidney compared to 4 weeks-old. This change increased to 59% for 4 weeks-old kidney compared to 34 weeks-old kidneys. Thus, these results show an increase in kidney OS with a longer duration of diabetes, indicating more severe diabetes in these kidney models.

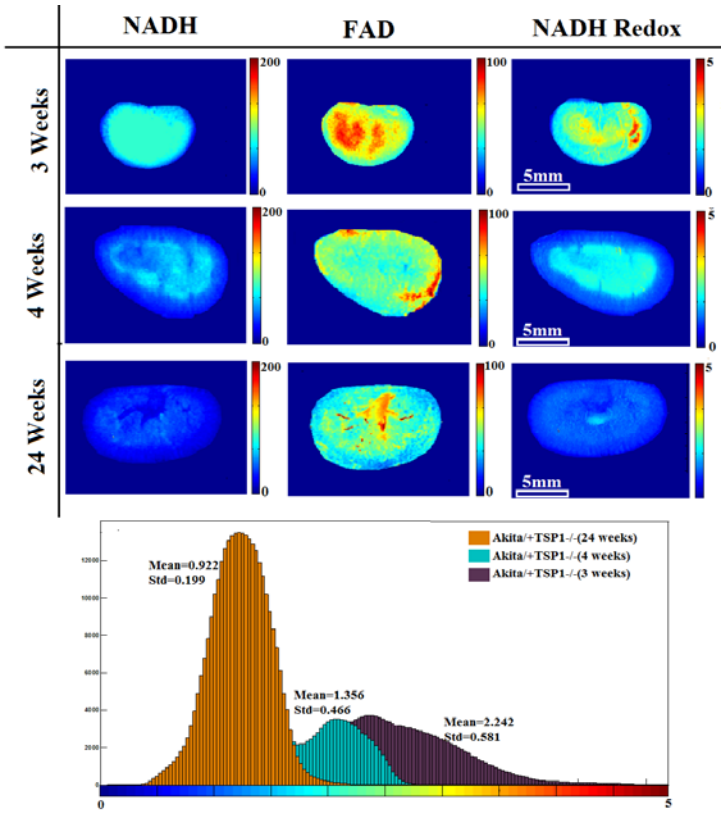

Figure 4.5. Representative Akita/+TSP1-/- kidney panel over age. Representative max projected NADH, FAD and NADH RR images and their related histograms for kidneys from 3, 4, and 24week-old Akita/+TSP1-/- kidneys.

Figure 4.6 displays a bar graph plot comparing the mean values of the NADH RR histograms of max projected images for kidneys from Akita/+ versus their appropriate control male littermates. The results show decreased NADH RR for all Akita/+ mice

compared with their non-diabetic control littermates, which becomes more significant in 12 and 34 weeks-old diabetic mouse kidneys.

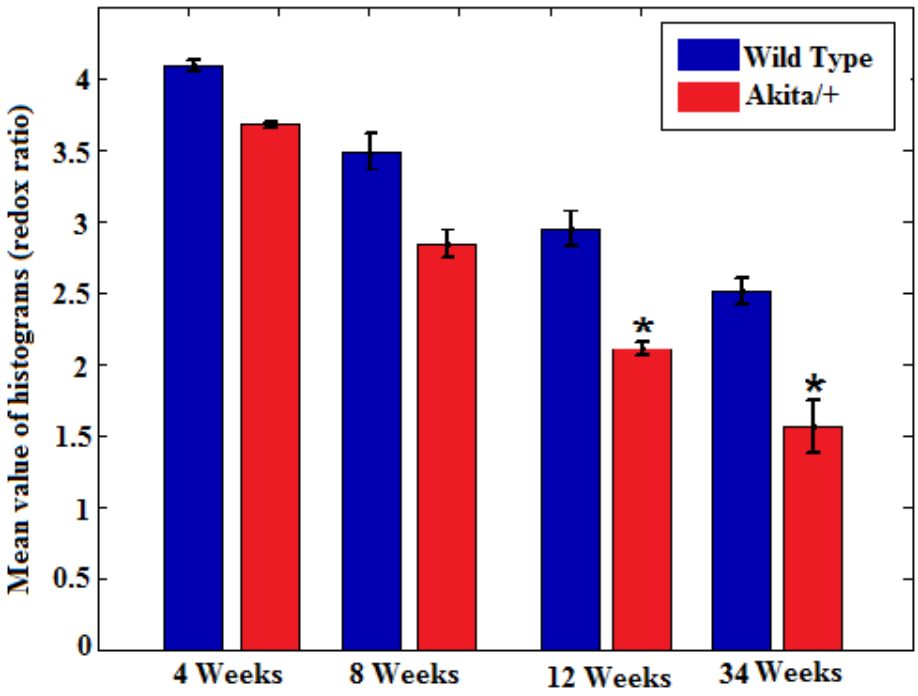

Figure 4.6. Bar graph plots for Akita/+ and WT kidneys. Bar graph plot comparing the mean values of the NADH RR histograms of max projected images from Akita/+ and their respective controls. The results show a significant difference between kidneys from 12 and 34 weeks-old non-diabetic and diabetic Akita/+ mice.

The result of the four groups of diabetic mice and their control littermates demonstrated different redox images, and the mean values in all four groups showed increased OS with the progression of diabetes. Thus, the significant difference in the mean NADH RR of kidneys from diabetic mice compared with their appropriate controls

indicates that the sensitivity of NADH RR can be used as a marker of renal OS. Since in the presence of excessive ROS due to diabetes, the mitochondrial coenzymes NADH and $FADH_2$ accumulate in their oxidized forms (NAD and FAD), mitochondrial NADH RR showed a decrease as a result of OS.

Figure 4.7 displays a bar graph plot comparing the mean values of the NADH RR histograms of max projected images for kidneys from Akita/+TSP1-/- versus their appropriate control littermates. The results show a more decreased NADH RR for all Akita/+TSP1-/- mice compared with their control littermates, which becomes more significant in 4 and 24 weeks-old diabetic mouse kidneys.

TSP1 is an endogenous inhibitor of angiogenesis. Therefore, changes in TSP1 levels during diabetes may contribute to the development and progression of diabetic nephropathy. The current study indicates that in the absence of TSP1, the development and progression of nephropathy is significantly expedited in a novel diabetic model. The results show that lack of TSP1 exacerbates the development and progression of early diabetic nephropathy using NADH RR as a quantitative marker of OS.

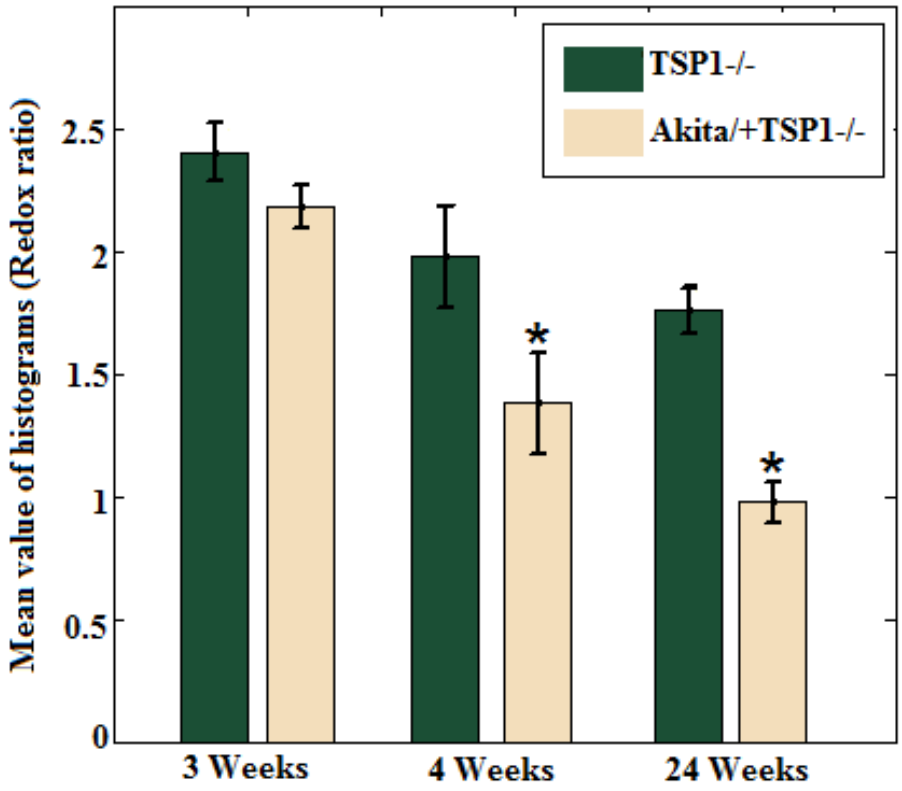

Figure 4.7. Bar graph plots for Akita/+ and WT kidneys. Bar graph plot comparing the mean values of the NADH RR histograms of max projected images from Akita/+TSP1-/- and their respective controls. The results show a significant difference between kidneys from 4 and 24 weeks.

Figure 4.8 displays a bar graph comparing the mean values of the NADH RR histograms of max projected images for kidneys from Akita/+ versus Akita/+TSP1-/- in different ages to show the severity of diabetes in the Akita/+TSP1-/- mice models. The results show a larger decrease in NADH RR for all Akita/+TSP1-/- mice compared with Akita/+ mice kidneys, which represents the higher OS and more severe diabetes in the Akita/+TSP1-/- mice models.

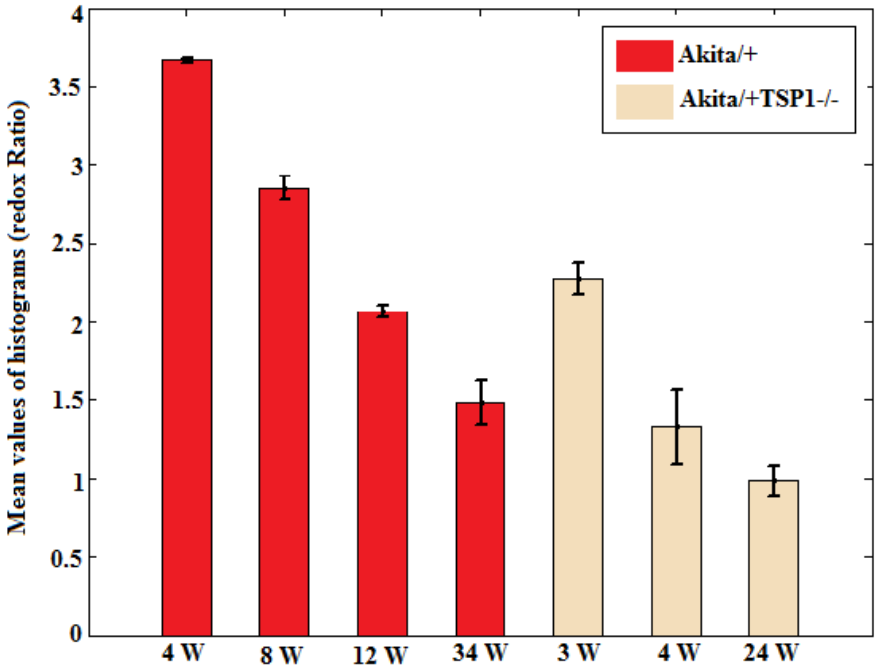

Figure 4.8. Bar graphs for Akita/+ and Akita/+TSP1-/- kidneys. Bar graph comparing the mean values of the NADH RR histograms of max projected images from Akita/+TSP1-/- and their respective controls. The results show a significant difference between kidneys from 4 and 24 weeks.

In the absence of TSP1, diabetes-related damage to the kidney occurred more rapidly, which translated to a further decrease in NADH RR compared with Akita/+ and enhanced renal complications. The Akita/+ phenotype (diabetic) is key to affecting NADH RR levels. The strong decrease in the mean value of Akita/+TSP1-/- as compared with Akita/+, combined with the fact that TSP1-/- does not itself decrease the mean value, provides evidence in support of the hypothesis that the lack of TSP1 exacerbates the pathogenesis of diabetic nephropathy. The results demonstrate the utility of cryoimaging for measuring kidney tissue mitochondrial redox state in different stages of

OS associated with the progression of diabetes. The NADH RR reveals differences in tissue NADH, FAD, and NADH RR signals between diabetic mice and their control littermates.

Chapter 5

Conclusion

5. Conclusion

I have studied diabetes cellular dysfunction in rodents kidney tissue by using and improving a 3-D optical imaging instrument called the cryoimager. The cryoimager allows measurement of mitochondrial redox state of biological tissue for diagnosis of nephropathy caused by diabetes. This technique was used to quantify the progression of the cellular dysfunction (due to oxidative stress) in three different diabetic models, to delineate the temporal distribution of OS during diabetes, and to detect the severity of diabetes.

The result of three groups of diabetic mice and their control demonstrated relative changes in mean value of redox ratio correlated with the severity of the disease. For example, in one model of diabetes (e.g. Akita) the mean NADH RR value differences in diseased and control animals increased from 8% to 15 % to 28% to 33% from 4 weeks to 8 weeks to 12 weeks and 34 weeks of the onset of diabetes. This difference in the mean NADH RR is due to an increase in OS with the progression of the disease. To account for the statistical significance, repeated experiments showed that we reached the significance in the 8and 12-weeks rodents with a $P<0.001$.

The future direction of this research is to add the capability of microscopy to our cryoimager for cellular-resolution imaging. Cellular imaging allows for the visualization and quantification of biological processes of the disease mechanism at the molecular and cellular levels. For instance, pericytes that are more specifically located surrounding the endothelial cell are affected during diabetes. These cellular images are used to

determine the quantity of endothelial cells and pericytes as well as extracting features from the structure of the vasculature and vasculature development, which are important factors in the development of diabetic retinopathy.

6. References

[1] A. O. Fred Ottoboni, *The modern nutritional diseases: and how to prevent them* vol. 3. United States of America: Vincente Books Inc., 2004.

[2] (2011). *Diabetes Statistics*. Available: http://www.diabetes.org/diabetes-basics/diabetes-statistics/?loc=DropDownDB-stats

[3] T. Vo-Dinh, *Biomedical photonics handbook.* Boca Raton, Fla: CRC Press, 2003.

[4] G. A. Wagnieres*, et al.*, "In vivo fluorescence spectroscopy and imaging for oncological applications," *Photochem Photobiol,* vol. 68, pp. 603-32, Nov 1998.

[5] J. R. Lakowicz, *Principles of Fluorescence spectroscopy*. New York: plenum press, 1985.

[6] B. R. Masters and B. chance, *Fluorescence and Luminescent probes for Biological Activity*. London: Academic Press, 1993.

[7] B. Alberts, *Molecular biology of the cell* vol. 4th ed. New York: Garland Science, 2002.

[8] B. Autran*, et al.*, "Positive effects of combined antiretroviral therapy on CD4+ T cell homeostasis and function in advanced HIV disease," *Science,* vol. 277, pp. 112-6, Jul 4 1997.

[9] C. N. A. B. W. R. J. Heyden, *Biology: Exploring Life*. Boston: Pearson Prentice Hall, 2006.

[10] (2004). *Animal Port*. Available: http://www.animalport.com/animal-cells.html

[11] E. N. M. a. K. Hoehn, *Human anatomy & physiology* vol. 8th ed. San Francisco: Benjamin Cummings, 2010.

[12] K. H. a. W. Martin, *Evolutionary biology: essence of mitochondria* vol. vol. 426: Nature, Nov 13 2003.

[13] N. R. Pace, *The universal nature of biochemistry* vol. 98, pp. 805-8,: Proc Natl Acad Sci U S A, Jan 30 2001.

[14] J. L. Spees*, et al.*, "Mitochondrial transfer between cells can rescue aerobic respiration," *Proc Natl Acad Sci U S A,* vol. 103, pp. 1283-8, Jan 31 2006.

[15] e. a. D. Voet, *Fundamentals of biochemistry : life at the molecular level* vol. 2nd ed: Wiley, 2006.

[16] (2010). *The Electron Transfer Chain*. Available: http://inoxx.net/?tag=electron-transport-chain

[17] T. M. Devlin, *Textbook of biochemistry : with clinical correlations* vol. 7th ed. Hoboken: John Wiley & Sons, 2011.

[18] N. Kango, *Textbook of Microbiology*. New Delhi: International Publishing House Pvt. Ltd, 2010.

[19] A. B. Fisher, *Intermediary metabolism of the lung* vol. vol. 55, pp. 149-58: Environ Health Perspect, Apr 1984.

[20] J. M. M. a. F. M. Sanchez-Jimenez, "Role of reactive oxygen species in apoptosis: implications for cancer therapy," *Int J Biochem Cell Biol,* vol. 32, pp. 157-70, Feb 2000.

[21] B. H. a. J. M. C. Gutteridge, *Free radicals in biology and medicine* vol. 4th ed. New York: Oxford University Press, 2007.

[22] G. Lenaz*, et al.*, "Mitochondria, oxidative stress, and antioxidant defences," *Acta Biochim Pol,* vol. 46, pp. 1-21, 1999.
[23] W. L. Yen and D. J. Klionsky, "How to live long and prosper: autophagy, mitochondria, and aging," *Physiology (Bethesda),* vol. 23, pp. 248-62, Oct 2008.
[24] T. M. Buttke and P. A. Sandstrom, "Oxidative stress as a mediator of apoptosis," *Immunol Today,* vol. 15, pp. 7-10, Jan 1994.
[25] (2012). *Basic Concepts in Fluorescence*. Available: http://micro.magnet.fsu.edu/primer/techniques/fluorescence/fluorescenceintro.htm
[26] (2011). *Stokes Shift*. Available: https://upload.wikimedia.org/wikipedia/commons/thumb/2/28/Stokes-Verschiebung.svg/430px-Stokes-Verschiebung.svg.png
[27] J. R. Gispert, *Coordination chemistry.*: Weinheim: Wiley-VCH, 2008.
[28] J. M. Christie*, et al.*, "LOV (light, oxygen, or voltage) domains of the blue-light photoreceptor phototropin (nph1): binding sites for the chromophore flavin mononucleotide," *Proc Natl Acad Sci U S A,* vol. 96, pp. 8779-83, Jul 20 1999.
[29] G. H. Patterson*, et al.*, "Separation of the glucose-stimulated cytoplasmic and mitochondrial NAD(P)H responses in pancreatic islet beta cells," *Proc Natl Acad Sci U S A,* vol. 97, pp. 5203-7, May 9 2000.
[30] B. Chance and H. Baltscheffsky, "Respiratory enzymes in oxidative phosphorylation. VII. Binding of intramitochondrial reduced pyridine nucleotide," *J Biol Chem,* vol. 233, pp. 736-9, Sep 1958.
[31] R. Sepehr*, et al.*, "Optical imaging of tissue mitochondrial redox state in intact rat lungs in two models of pulmonary oxidative stress," *J Biomed Opt,* vol. 17, p. 046010, Apr 2012.
[32] M. Ranji*, et al.*, "Fluorescence spectroscopy and imaging of myocardial apoptosis," *J Biomed Opt,* vol. 11, p. 064036, Nov-Dec 2006.
[33] M. Ranji*, et al.*, "Quantifying acute myocardial injury using ratiometric fluorometry," *IEEE Trans Biomed Eng,* vol. 56, pp. 1556-63, May 2009.
[34] B. Chance*, et al.*, "Oxidation-reduction ratio studies of mitochondria in freeze-trapped samples. NADH and flavoprotein fluorescence signals," *J Biol Chem,* vol. 254, pp. 4764-71, Jun 10 1979.
[35] e. a. Y. Avi-Dor, "Fluorescence of Pyridine Nucleotides in Mitochondria," *J Biol Chem,* vol. 237, pp. 2377-2383, 1962.
[36] L. K. Klaidman*, et al.*, "High-performance liquid chromatography analysis of oxidized and reduced pyridine dinucleotides in specific brain regions," *Anal Biochem,* vol. 228, pp. 312-7, Jul 1 1995.
[37] e. a. M. O'Connor, "Origin of labile NADH tissue fluorescence," *Oxygen Physiol. Function,* vol. 10, p. 10, 1977.
[38] B. Chance*, et al.*, "Intracellular oxidation-reduction states in vivo," *Science,* vol. 137, pp. 499-508, Aug 17 1962.
[39] S. Wan*, et al.*, "Transmittance of nonionizing radiation in human tissues," *Photochem Photobiol,* vol. 34, pp. 679-81, Dec 1981.
[40] J. Lee*, et al.*, "Noninvasive in vivo monitoring of cyanide toxicity and treatment using diffuse optical spectroscopy in a rabbit model," *Mil Med,* vol. 174, pp. 615-21, Jun 2009.

[41] O. Coquoz, *et al.*, "Optical property measurements of turbid media in a small-volume cuvette with frequency-domain photon migration," *Appl Opt,* vol. 40, pp. 6281-91, Dec 1 2001.
[42] S. Andersson-Engels, *et al.*, "In vivo fluorescence imaging for tissue diagnostics," *Phys Med Biol,* vol. 42, pp. 815-24, May 1997.
[43] H. Stepp, *et al.*, "Fluorescence endoscopy of gastrointestinal diseases: basic principles, techniques, and clinical experience," *Endoscopy,* vol. 30, pp. 379-86, May 1998.
[44] K. T. Moesta, *et al.*, "Protoporphyrin IX occurs naturally in colorectal cancers and their metastases," *Cancer Res,* vol. 61, pp. 991-9, Feb 1 2001.
[45] J. M. Maarek, *et al.*, "Time-resolved fluorescence spectra of arterial fluorescent compounds: reconstruction with the Laguerre expansion technique," *Photochem Photobiol,* vol. 71, pp. 178-87, Feb 2000.
[46] C. H. Barlow, *et al.*, "Fluorescence mapping of mitochondrial redox changes in heart and brain," *Crit Care Med,* vol. 7, pp. 402-6, Sep 1979.
[47] E. Meirovithz, *et al.*, "Effect of hyperbaric oxygenation on brain hemodynamics, hemoglobin oxygenation and mitochondrial NADH," *Brain Res Rev,* vol. 54, pp. 294-304, Jun 2007.
[48] R. S. Balaban and L. J. Mandel, "Coupling of aerobic metabolism to active ion transport in the kidney," *J Physiol,* vol. 304, pp. 331-48, Jul 1980.
[49] S. Maleki, *et al.*, "Mitochondrial redox studies of oxidative stress in kidneys from diabetic mice," *Biomed Opt Express,* vol. 3, pp. 273-81, Feb 1 2012.
[50] B. Vollmar, *et al.*, "A correlation of intravital microscopically assessed NADH fluorescence, tissue oxygenation, and organ function during shock and resuscitation of the rat liver," *Adv Exp Med Biol,* vol. 454, pp. 95-101, 1998.
[51] S. Nioka, *et al.*, "Simulation of Mb/Hb in NIRS and oxygen gradient in the human and canine skeletal muscles using H-NMR and NIRS," *Adv Exp Med Biol,* vol. 578, pp. 223-8, 2006.
[52] N. Ramanujam, *et al.*, "In vivo diagnosis of cervical intraepithelial neoplasia using 337-nm-excited laser-induced fluorescence," *Proc Natl Acad Sci U S A,* vol. 91, pp. 10193-7, Oct 11 1994.
[53] e. a. M. Ranji, "Fluorescent images of mitochondrial redox states of in situ mouse hypoxic ischemic intestines," *J Innov Opt Health Sci,* vol. 2, pp. 365-374, 2009.
[54] e. a. R. Sepehr, "Fluorescence Spectroscopy and Cryoimaging of Rat Lung Tissue Mitochondrial Redox State," *SPIE, Munich,* 2011.
[55] M. D. Breyer, *et al.*, "Mouse models of diabetic nephropathy," *J Am Soc Nephrol,* vol. 16, pp. 27-45, Jan 2005.
[56] G. L. King and M. R. Loeken, "Hyperglycemia-induced oxidative stress in diabetic complications," *Histochem Cell Biol,* vol. 122, pp. 333-8, Oct 2004.
[57] J. S. Johansen, *et al.*, "Oxidative stress and the use of antioxidants in diabetes: linking basic science to clinical practice," *Cardiovasc Diabetol,* vol. 4, p. 5, 2005.
[58] T. Inoue, *et al.*, "Noninvasive evaluation of kidney hypoxia and fibrosis using magnetic resonance imaging," *J Am Soc Nephrol,* vol. 22, pp. 1429-34, Aug 2011.
[59] L. Piconi, *et al.*, "Oxidative stress in diabetes," *Clin Chem Lab Med,* vol. 41, pp. 1144-9, Sep 2003.

[60] M. M. Delmastro and J. D. Piganelli, "Oxidative stress and redox modulation potential in type 1 diabetes," *Clin Dev Immunol,* vol. 2011, p. 593863, 2011.
[61] W. I. Sivitz and M. A. Yorek, "Mitochondrial dysfunction in diabetes: from molecular mechanisms to functional significance and therapeutic opportunities," *Antioxid Redox Signal,* vol. 12, pp. 537-77, Apr 2010.
[62] C. J. Mullarkey, *et al.*, "Free radical generation by early glycation products: a mechanism for accelerated atherogenesis in diabetes," *Biochem Biophys Res Commun,* vol. 173, pp. 932-9, Dec 31 1990.
[63] T. Nishikawa, *et al.*, "Normalizing mitochondrial superoxide production blocks three pathways of hyperglycaemic damage," *Nature,* vol. 404, pp. 787-90, Apr 13 2000.
[64] D. A. Greene, *et al.*, "Glucose-induced oxidative stress and programmed cell death in diabetic neuropathy," *Eur J Pharmacol,* vol. 375, pp. 217-23, Jun 30 1999.
[65] N. Sheibani, *et al.*, "Bcl-2 expression modulates cell adhesion and migration promoting branching of ureteric bud cells," *J Cell Physiol,* vol. 210, pp. 616-25, Mar 2007.
[66] E. R. Seaquist, *et al.*, "Familial clustering of diabetic kidney disease. Evidence for genetic susceptibility to diabetic nephropathy," *N Engl J Med,* vol. 320, pp. 1161-5, May 4 1989.
[67] S. Araki, *et al.*, "APOE polymorphisms and the development of diabetic nephropathy in type 1 diabetes: results of case-control and family-based studies," *Diabetes,* vol. 49, pp. 2190-5, Dec 2000.
[68] J. E. Klaunig, *et al.*, "The role of oxidative stress in chemical carcinogenesis," *Environ Health Perspect,* vol. 106 Suppl 1, pp. 289-95, Feb 1998.
[69] I. Rahman, *et al.*, "Oxidant and antioxidant balance in the airways and airway diseases," *Eur J Pharmacol,* vol. 533, pp. 222-39, Mar 8 2006.
[70] S. P. Wolff and R. T. Dean, "Glucose autoxidation and protein modification. The potential role of 'autoxidative glycosylation' in diabetes," *Biochem J,* vol. 245, pp. 243-50, Jul 1 1987.
[71] A. K. Zimmermann, *et al.*, "Glutathione binding to the Bcl-2 homology-3 domain groove: a molecular basis for Bcl-2 antioxidant function at mitochondria," *J Biol Chem,* vol. 282, pp. 29296-304, Oct 5 2007.
[72] I. Giardino, *et al.*, "BCL-2 expression or antioxidants prevent hyperglycemia-induced formation of intracellular advanced glycation endproducts in bovine endothelial cells," *J Clin Invest,* vol. 97, pp. 1422-8, Mar 15 1996.
[73] N. Susnow, *et al.*, "Bcl-2 family proteins as regulators of oxidative stress," *Semin Cancer Biol,* vol. 19, pp. 42-9, Feb 2009.
[74] Y. Ueno, *et al.*, "Increase in oxidative stress in kidneys of diabetic Akita mice," *Biosci Biotechnol Biochem,* vol. 66, pp. 869-72, Apr 2002.
[75] S. L. Bernard, *et al.*, "High spatial resolution measurements of organ blood flow in small laboratory animals," *Am J Physiol Heart Circ Physiol,* vol. 279, pp. H2043-52, Nov 2000.

[76] J. R. E. J. J. Kelly, S. L. Bernard, R. W. Glenny, and C. H. Barlow, "Regional blood flow measurements from fluorescent microsphere images using an Imaging CryoMicrotome," *Rev Sci Instrum,* vol. 71, pp. 228-234, 2000.
[77] (2012). *QIMAGING Aqua color camera*. Available: http://www.qimaging.com/products/cameras/scientific/exi_aqua.php
[78] (2012). *Pentax lens*. Available: http://www.pentaximaging.com/camera-lenses/
[79] (2012). *Rolera monochrom camera*. Available: http://www.qimaging.com/products/cameras/scientific/
[80] (2012). *Canon lens*. Available: http://www.usa.canon.com/cusa/consumer/products/cameras/ef_lens_lineup
[81] (2012). *Spectral intensity of mercury-arc lamp*. Available: http://zeiss-campus.magnet.fsu.edu/articles/lightsources/mercuryarc.html

7. Appendix

This section contains the abstracts of the three publications related to this thesis.

Biomedical Optics EXPRESS

Mitochondrial redox studies of oxidative stress in kidneys from diabetic mice

Sepideh Maleki,[1] Reyhaneh Sepehr,[1] Kevin Staniszewski,[1] Nader Sheibani,[2] Christine M. Sorenson,[3] and Mahsa Ranji[1,*]

[1]*Biophotonics Laboratory, University of Wisconsin Milwaukee, Department of Electrical Engineering and Computer Science, 3200 N Cramer St., Milwaukee, WI 53211-3029, USA*
[2]*Departments of Ophthalmology and Visual Sciences, University of Wisconsin School of Medicine and Public Health, 600 Highland Avenue, Madison, WI, 53792-4673, USA*
[3]*Department of Pediatrics, University of Wisconsin School of Medicine and Public Health, 600 Highland Avenue, Madison, WI, 53792-4673, USA*
**ranji@uwm.edu*

Abstract: Chronic hyperglycemia during diabetes leads to increased production of reactive oxygen species (ROS) and increased oxidative stress (OS). Here we investigated whether changes in the metabolic state can be used as a marker of OS progression in kidneys. We examined redox states of kidneys from diabetic mice, Akita$^{/+}$ and Akita$^{/+}$;TSP1$^{-/-}$ mice (Akita mice lacking thrombospondin-1, TSP1) with increasing duration of diabetes. OS as measured by mitochondrial redox ratio (NADH/FAD) was detectable shortly after the onset of diabetes and further increased with the duration of diabetes. Thus, cryo fluorescence redox imaging was used as a quantitative marker of OS progression in kidneys from diabetic mice and demonstrated that alterations in the oxidative state of kidneys occur during the early stages of diabetes.

OCIS codes: (260.2510) Fluorescence; (000.1430) Biology and medicine; (170.0110) Imaging systems; (170.3880) Medical and biological imaging; (170.6280) Spectroscopy, fluorescence and luminescence; (100.2960) Image analysis.

References and links

1. N. Sheibani, E. A. Scheef, T. A. Dimaio, Y. Wang, S. Kondo, and C. M. Sorenson, "Bcl-2 expression modulates cell adhesion and migration promoting branching of ureteric bud cells," J. Cell. Physiol. **210**(3), 616–625 (2007).
2. J. S. Johansen, A. K. Harris, D. J. Rychly, and A. Ergul, "Oxidative stress and the use of antioxidants in diabetes: linking basic science to clinical practice," Cardiovasc. Diabetol. **4**(1), 5–9999 (2005).
3. L. Piconi, L. Quagliaro, and A. Ceriello, "Oxidative stress in diabetes," Clin. Chem. Lab. Med. **41**(9), 1144–1149 (2003).
4. M. D. Breyer, E. Böttinger, F. C. Brosius 3rd, T. M. Coffman, R. C. Harris, C. W. Heilig, and K. Sharma; AMDCC, "Mouse models of diabetic nephropathy," J. Am. Soc. Nephrol. **16**(1), 27–45 (2005).
5. A. Ceriello, S. Kumar, L. Piconi, K. Esposito, and D. Giugliano, "Simultaneous control of hyperglycemia and oxidative stress normalizes endothelial function in type 1 diabetes," Diabetes Care **30**(3), 649–654 (2007).
6. Y. Ueno, F. Horio, K. Uchida, M. Naito, H. Nomura, Y. Kato, T. Tsuda, S. Toyokuni, and T. Osawa, "Increase in oxidative stress in kidneys of diabetic Akita mice," Biosci. Biotechnol. Biochem. **66**(4), 869–872 (2002).
7. M. M. Delmastro and J. D. Piganelli, "Oxidative stress and redox modulation potential in type 1 diabetes," Clin. Dev. Immunol. **2011**, 593863 (2011).
8. W. I. Sivitz and M. A. Yorek, "Mitochondrial dysfunction in diabetes: from molecular mechanisms to functional significance and therapeutic opportunities," Antioxid. Redox Signal. **12**(4), 537–577 (2010).
9. I. Giardino, D. Edelstein, and M. Brownlee, "Bcl-2 expression or antioxidants prevent hyperglycemia-induced formation of intracellular advanced glycation endproducts in bovine endothelial cells," J. Clin. Invest. **97**(6), 1422–1428 (1996).
10. S. S. Chung, E. C. Ho, K. S. Lam, and S. K. Chung, "Contribution of polyol pathway to diabetes-induced oxidative stress," J. Am. Soc. Nephrol. **14**(Suppl 3), S233–S236 (2003).
11. G. L. King and M. R. Loeken, "Hyperglycemia-induced oxidative stress in diabetic complications," Histochem. Cell Biol. **122**(4), 333–338 (2004).
12. H. Bugger, S. Boudina, X. X. Hu, J. Tuinei, V. G. Zaha, H. A. Theobald, U. J. Yun, A. P. McQueen, B. Wayment, S. E. Litwin, and E. D. Abel, "Type 1 diabetic Akita mouse hearts are insulin sensitive but manifest

#158659 - $15.00 USD Received 23 Nov 2011; revised 16 Dec 2011; accepted 1 Jan 2012; published 10 Jan 2012

Optical imaging of tissue mitochondrial redox state in intact rat lungs in two models of pulmonary oxidative stress

Reyhaneh Sepehr,[a] Kevin Staniszewski,[a] Sepideh Maleki,[a] Elizabeth R. Jacobs,[b] Said Audi,[b,c] and Mahsa Ranji[a]
[a]University of Wisconsin Milwaukee, Biophotonics Lab, Department of Electrical Engineering, Milwaukee, Wisconsin 53211
[b]Pulmonary Division, Zablocki VA Medical Center, Milwaukee, Wisconsin 53295
[c]Marquette University, Department of Biomedical Engineering, Milwaukee, Wisconsin 53233

Abstract. Ventilation with enhanced fractions of O_2 (hyperoxia) is a common and necessary treatment for hypoxemia in patients with lung failure, but prolonged exposure to hyperoxia causes lung injury. Ischemia-reperfusion (IR) injury of lung tissue is common in lung transplant or crush injury to the chest. These conditions are associated with apoptosis and decreased survival of lung tissue. The objective of this work is to use cryoimaging to evaluate the effect of exposure to hyperoxia and IR injury on lung tissue mitochondrial redox state in rats. The autofluorescent mitochondrial metabolic coenzymes nicotinamide adenine dinucleotide (NADH) and flavin adenine dinucleotide (FAD) are electron carriers in ATP generation. These intrinsic fluorophores were imaged for rat lungs using low-temperature fluorescence imaging (cryoimaging). Perfused lungs from four groups of rats were studied: normoxia (control), control perfused with an mitochondrial complex IV inhibitor (potassium cyanide, KCN), rats exposed to hyperoxia (85% O_2) for seven days, and from rats subjected to lung IR *in vivo* 24 hours prior to study. Each lung was sectioned sequentially in the transverse direction, and the images were used to reconstruct a three-dimensional (3-D) rendering. In KCN perfused lungs the respiratory chain was more reduced, whereas hyperoxic and IR lung tissue have a more oxidized respiratory chain than control lung tissue, consistent with previously measured mitochondrial dysfunction in both hyperoxic and IR lungs. [DOI: 10.1117/1.JBO.17.4.046010]

Keywords: optical imaging; nicotinamide adenine dinucleotide; flavin adenine dinucleotide; mitochondrial redox; lung tissue; hyperoxia; ischemia-reperfusion.

Paper 11581 received Oct. 7, 2011; revised manuscript received Feb. 3, 2012; accepted for publication Feb. 14, 2012; published online Apr. 19, 2012.

1 Introduction

Fluorescence imaging techniques provide both anatomical and functional information of tissue via intrinsic fluorophores or exogenous tagged proteins.[1] These techniques are widely used to probe tissue redox state and energy homeostasis in organs such as the heart,[2] brain,[3] kidney,[4–6] liver,[7] skeletal muscle,[8] cervix,[9] and colon,[10] as well as to diagnose diseases, such as breast cancer tumor localization and oxygenation.[11,12] Furthermore, these techniques have been shown to have a high sensitivity and specificity for discriminating between diseased and nondiseased tissue.[13]

Tissue metabolic state, which is an indicator of cellular oxygen consumption, can be extracted from fluorescence images of intrinsic fluorophores.[14,15] The mitochondrial metabolic coenzymes nicotinamide adenine dinucleotide (NADH) and flavin adenine dinucleotide ($FADH_2$) are the primary electron carriers in oxidative phosphorylation. NADH and $FADH_2$ oxidation via the electron transport chain results in the translocation of protons from complexes I, III, and IV across the inner mitochondrial membrane into the mitochondrial inner membrane region. The resulting proton gradient across the inner mitochondrial membrane, along with adenosine diphosphate (ADP) availability, controls the rate of mitochondrial adenosine triphosphate (ATP) synthesis, which accounts for ~90% of ATP production in lung tissue. Thus, a change in redox ratio (RR) is an index of a change in lung tissue bioenergetics.[16]

NADH and FAD (oxidized form of $FADH_2$) are autofluorescent and can be monitored without exogenous labels by noninvasive optical techniques.[17] The fluorescence signals of these intrinsic fluorophores have been used as indicators of tissue metabolism in injuries due to hypoxia, ischemia, and cell death.[18] Ranji et al. demonstrated that the ratio of these fluorophores, termed the mitochondrial redox ratio (RR = NADH/FAD), is a marker of the mitochondrial redox and metabolic state of myocardial tissue in intact hearts or *in vivo* situations.[19–22] There is more than one definition for redox ratio, including the normalized redox ratio [NADH/(NADH + FAD)];[18] the definition that is used in this study (NADH/FAD) is chosen since the FAD signal in lung tissue, as compared to the NADH signal, is significantly smaller than in other organ tissues such as the heart. Thus, the normalized redox ratio would be less sensitive to a change in mitochondrial redox state than NADH/FAD.

Rapid freeze trapping of organs in liquid nitrogen temperatures preserves the tissue metabolic state. Subsequent low-temperature fluorescence imaging (cryoimaging) is advantageous since it provides high fluorescence quantum yield of NADH and FAD as compared with room temperature, and 3-D spatial distribution of tissue NADH and FAD fluorescence intensities.[21,23,24]

Address all correspondence to: Mahsa Ranji, University of Wisconsin Milwaukee, Biophotonics Lab, Department of Electrical Engineering, , Milwaukee, Wisconsin 53211. Tel: 414-229-6619; Fax: 414-229-6958; E-mail: ranji@uwm.edu

0091-3286/2012/$25.00 © 2012 SPIE

Optical cryoimaging of kidney mitochondrial redox state in diabetic mice models

S. Maleki[a], R. Sepehr[a], K. Staniszewski[a], N. Sheibani[b] C.M. Sorenson[c], M. Ranji*[a]
[a]Biophotonics Laboratory, Dept. of Electrical Engineering, University of Wisconsin Milwaukee, 3200 N Cramer St., Milwaukee, WI, USA 53211-3029
[b]Dept. of Ophthalmology and Visual Sciences, University of Wisconsin School of Medicine and Public Health, 600 Highland Avenue, Madison, WI, USA 53792-4673
[c]Dept. of Pediatrics, University of Wisconsin School of Medicine and Public Health, 600 Highland Avenue, Madison, WI, USA 53792-4673

ABSTRACT

Oxidative stress (OS), which increases during diabetes, exacerbates the development and progression of diabetes complications including renal vascular and proximal tubule cell dysfunction. The objective of this study was to investigate the changes in the metabolic state of the tissue in diabetic mice kidneys using fluorescence imaging. Mitochondrial metabolic coenzymes NADH (Nicotinamide Adenine Dinucleotide), and FADH-2 (Flavin Adenine Dinucleotide) are autofluorescent and can be monitored without exogenous labels by optical techniques. The ratio of the fluorescence intensity of these fluorophores, (NADH/FAD), called the NADH redox ratio (RR), is a marker of metabolic state of a tissue. We examined mitochondrial redox states of kidneys from diabetic mice, Akita/+ and its control wild type (WT) for a group of 8- and 12-week-old mice. Average intensity and histogram of maximum projected images of FAD, NADH, and NADH RR were calculated for each kidney. Our results indicated a 17% decrease in the mean NADH RR of the kidney from 8-week-old mice compared with WT mice and, a 30% decrease in the mean NADH RR of kidney from12–week-old mice compared with WT mice. These results indicated an increase in OS in diabetic animals and its progression over time. Thus, NADH RR can be used as a hallmark of OS in diabetic kidney allowing temporal identification of oxidative state.

Keywords: Oxidative stress, diabetes, hyperglycemia, Akita diabetic mouse model, NADH redox ratio, fluorescence imaging.

1. INTRODUCTION

Diabetic nephropathy (DN), which is a progressive kidney disease, accounts as a common cause of end stage renal disease (ESRD) and a major risk factor for cardiovascular disease [1-5]. Chronic hyperglycemia during diabetes can trigger excess generation of reactive oxygen species (ROS) and increased oxidative stress (OS). OS in turn may play a key role in causing DNA damage, cell death, and protein modifications that result in mitochondrial dysfunction. Diabetes, a common metabolic disorder, causes an increase in OS in various tissues such as kidneys from diabetic Akita mice [3, 6-8]. Akita diabetic mice develop type 1 diabetes as early as 4-weeks of age. ROS observed in the diabetic kidney is due to enzymatic and non-enzymatic sources such as advanced glycation, mitochondrial respiration chain deficiencies and NAD(P)H oxidase. Redox state of the cell is usually defined as the balance between oxidative species production and antioxidant protection of the cells. An imbalance between ROS production and anti-oxidant action of the cells results in OS production [1, 5, 9-11]. Therefore, the cellular oxygen consumption can be evaluated from tissue metabolic state, and it can be extracted from fluorescence images [12, 13]. In this study, the OS progression in diabetic Akita mice kidney tissue and its control wild type mice was assessed by a quantitative marker using mitochondrial intrinsic signals. Mitochondrial

* ranji@uwm.edu; Phone: (414) 229 5889; https://pantherfile.uwm.edu/ranji/www/

Imaging, Manipulation, and Analysis of Biomolecules, Cells, and Tissues X, edited by Daniel L. Farkas, Dan V. Nicolau, Robert C. Leif, Proc. of SPIE Vol. 8225, 82252A · © 2012 SPIE · CCC code: 1605-7422/12/$18 · doi: 10.1117/12.909394